



CHALMERS
UNIVERSITY OF TECHNOLOGY

A new Time-of-flight detector for the R 3 B setup

Downloaded from: <https://research.chalmers.se>, 2024-04-19 10:53 UTC

Citation for the original published paper (version of record):

Heil, M., Kelić-Heil, A., Bott, L. et al (2022). A new Time-of-flight detector for the R 3 B setup. European Physical Journal A, 58(12). <http://dx.doi.org/10.1140/epja/s10050-022-00875-8>

N.B. When citing this work, cite the original published paper.



A new Time-of-flight detector for the R³B setup

M. Heil^{1,a}, A. Kelić-Heil¹, L. Bott², T. Almusidi³, H. Alvarez-Pol⁴, L. Atar⁵, L. Atkins³, T. Aumann^{1,5}, J. Benlliure⁴, K. Boretzky¹, B. Brückner², P. Cabanelas⁴, C. Caesar¹, E. Casarejos⁷, J. Cederkall⁸, L. Chulkov⁹, A. Corsi¹⁰, J. Dueñas¹¹, P. Erbacher², S. Escribano Rodríguez³, A. Falduto⁵, M. Feijoo⁴, A. Frotscher¹², J. Frühauf¹, I. Gašparić¹³, M. J. G. Borge¹⁴, J. Gerbig², R. Gernhäuser¹⁵, M. Gilbert², J. Glorius¹, B. Gnoffo^{16,23}, K. Göbel², D. Gonzalez Caamaño⁴, A. Grein², A.-L. Hartig⁵, H. Heggen¹, M. Heine^{5,17}, A. Heinz⁶, M. Holl⁵, I. Homm⁵, A. Horvat⁵, H. T. Johansson⁶, B. Jonson⁶, N. Kalantar-Nayestanaki¹⁸, A. Kamenyero¹⁹, A. Khodaparast², O. Kiselev¹, P. Klenze¹⁵, M. Knösel⁵, K. Koch¹, D. Körper¹, T. Kröll⁵, D. Kurtulgil², N. Kurz¹, B. Löher¹, C. Langer^{2,20}, C. Lehr⁵, Y. Litvinov¹, H. Liu⁵, S. Murillo Morales³, E. Nácher²⁵, T. Nilsson⁶, J. Park^{8,24}, S. Paschalis³, L. Pellegrini^{21,22}, A. Perea¹⁴, M. Petri³, T. Pohl⁵, L. Ponnath¹⁵, R. Popočovski¹³, R. Reifarh², H.-B. Rhee⁵, J. L. Rodriguez Sanchez⁴, D. Rossi^{1,5}, C. Sürder⁵, A. M. Sánchez-Benítez¹¹, D. Savran¹, H. Scheit⁵, H. Simon¹, Z. Slavkovská², S. Storck-Dutine⁵, Y. Sun⁵, H. T. Törnqvist^{1,5}, J. Tanaka⁵, O. Tengblad¹⁴, B. Thomas², L. Varga¹, M. Volkandt², V. Wagner⁵, F. Wamers¹, L. Zanetti⁵, R³B collaboration

¹ GSI Helmholtzzentrum für Schwerionenforschung, Planckstraße 1, 64291 Darmstadt, Germany

² Goethe-Universität Frankfurt, Max-von-Laue Str. 1, 60438 Frankfurt am Main, Germany

³ Department of Physics, University of York, York YO10 5DD, UK

⁴ IGFAE, Universidade de Santiago de Compostela, 15782 Santiago de Compostela, Spain

⁵ Fachbereich Physik, Institut für Kernphysik, Technische Universität Darmstadt, 64289 Darmstadt, Germany

⁶ Department of Physics, Chalmers University of Technology, 41296 Göteborg, Sweden

⁷ CINTECX, Universidade de Vigo, DSN, Dpt. Mech. Engineering, E-36310 Vigo, Spain

⁸ Lund University, Lund, Sweden

⁹ NRC Kurchatov Institute-Moscow, pl. Akademika Kurchatova, Moscow, Russia

¹⁰ CEA Saclay, IRFU/DPhN, Centre de Saclay, 91191 Gif-sur-Yvette, France

¹¹ Depto. CC. Integradas y Centro de Estudios Avanzados en Física, Matemáticas y Computación. Fac. de CC. Experimentales, Universidad de Huelva, 21071 Huelva, Spain

¹² Institute of Radiation Physics, Helmholtz-Zentrum Dresden-Rossendorf, 01314 Dresden, Germany

¹³ RBI Zagreb, Bijenicka cesta 54, 10000 Zagreb, Croatia

¹⁴ Instituto de Estructura de la Materia, CSIC, 28006 Madrid, Spain

¹⁵ Technische Universität München, James-Franck-Str 1, 85748 Garching, Germany

¹⁶ Dipartimento di Fisica e Astronomia “Ettore Majorana”, Università di Catania, Catania, Italy

¹⁷ Institut Pluridisciplinaire Hubert CURIE, Schiltigheim, France

¹⁸ University of Groningen-ESRIG, Nuclear Energy Group, Groningen, The Netherlands

¹⁹ GANIL, Bd Henri Becquerel, 14076 Caen, France

²⁰ University of Applied Science Aachen, Fachbereich 10-Energietechnik, Physik/Kernphysik, Heinrich-Mußmann-Straße 1, 52428 Jülich, Germany

²¹ iThemba LABS, Faure 7131, South Africa

²² School of Physics, University of the Witwatersrand, Johannesburg 2050, South Africa

²³ INFN Sezione di Catania, Via Santa Sofia 64, Catania 95123, Italy

²⁴ Institute for Basic Science, Center for Exotic Nuclear Studies, Daejeon 34126, Korea

²⁵ Instituto de Física Corpuscular, CSIC-Universidad de Valencia, E-46980 Paterna, Valencia, Spain

Received: 25 July 2022 / Accepted: 31 October 2022

© The Author(s) 2022

Communicated by N. Alamanos

Abstract We present the design, prototype developments and test results of the new time-of-flight detector (ToFD) which is part of the R³B experimental setup at GSI and FAIR,

The members of R³B Collaboration are listed in Acknowledgements.

^a e-mail: M.Heil@gsi.de (corresponding author)

Darmstadt, Germany. The ToFD detector is able to detect heavy-ion residues of all charges at relativistic energies with a relative energy precision $\sigma_{\Delta E}/\Delta E$ of up to 1% and a time precision of up to 14 ps (sigma). Together with an elaborate particle-tracking system, the full identification of relativistic

ions from hydrogen up to uranium in mass and nuclear charge is possible.

1 Introduction

Detectors made of organic plastic scintillation materials are commonly used in nuclear physics experiments to measure time-of-flight, hit position, and energy loss of traversing ions. The intrinsic detection efficiency is typically 100%, these detectors are available at low cost and are easy to handle. Their properties, like scintillation-light emission wavelength and decay times, match the requirements given by modern nuclear-physics setups and, thus, are an ideal choice for many experiments at various facilities.

In this paper, we present the design, construction and performance of the new time-of-flight detector (ToFD) that consists of plastic scintillator bars and will be deployed at the R³B (Reactions with Relativistic Radioactive Beams) setup at GSI Helmholtzzentrum für Schwerionenforschung in Darmstadt, Germany.

1.1 The R³B setup

R³B is a versatile setup for nuclear-physics experiments in inverse kinematics at relativistic energies. This setup provides high efficiency, large acceptance, and high resolution for kinematically complete studies of reactions involving heavy-ion beams of short-lived nuclei. The physics program of the R³B collaboration is dedicated to reaction studies, with emphasis on nuclear structure, astrophysics and nuclear dynamics; technical applications are also considered.

The setup will be located at the focal plane of the high-energy branch of the Super-FRS [1,2] at FAIR, which will deliver high-quality secondary beams up to uranium at intensities ranging from a few hundred to several million particles/second. The experimental setup of R³B is configured to accept the highest beam energies provided by the Super-FRS corresponding to 20 Tm magnetic rigidity, capitalizing on the highest possible transmission of secondary beams.

The R³B setup has been designed and built by the R³B collaboration on the basis of more than 20 years of experience with the reaction setup LAND [3] at GSI, introducing substantial improvements with respect to resolution and an extended detection scheme.

One of the major improvements is the new large-acceptance super-conducting dipole magnet GLAD [4], which allows to perform experiments with beams with a rigidity up to 20 Tm. For nuclei in the lead-uranium region, this corresponds to kinetic energies of 1 GeV/nucleon at which the ions are fully stripped, thus, enabling unambiguous identification of the reaction products.

In order to fully exploit the potential of FAIR beams at the R³B setup - heavy beams and high intensities - the planned detector systems have to be able to cope with such new conditions.

The layout of the R³B experimental setup is sketched in Fig. 1. To perform kinematically complete measurements, it is mandatory to detect all particles emerging from the reaction - photons, neutrons, light-charged particles and heavy residues on an event-by-event basis. The key components of the setup are a station for tracking and identification of the incoming beam, the target area surrounded by the R³B silicon tracker [5] and the gamma-ray and light charged-particle calorimeter CALIFA [6], the super-conducting large-acceptance dipole magnet GLAD, the large-area neutron detector NeuLAND [7], the fragment and the proton arms with tracking and time-of-flight detectors [8]. For a detailed explanation of the setup and the physics program we refer the reader to the R³B Letter-of-Intent [9].

1.2 A new time-of-flight wall

The ToFD detector, made from plastic scintillators, will be situated about 20 m down-stream from the reaction target, behind the large dipole magnet GLAD. It will serve for a list of major tasks for a large variety of experiments performed at R³B. All heavy fragments produced in the reaction target will be recorded in the ToFD detector. Their specific energy loss and arrival time at the detector plane are essential for their identification in mass and nuclear charge. In addition, the detector will be one of the main trigger sources for the entire setup, it will measure the time between consecutive events to avoid event mixing, and it will provide absolute position information for the alignment of the whole tracking system.

In the following, the requirements, construction, working principles, and tests with a fast LED, laser and ion beams will be presented.

2 Design goals

Detectors based on plastic scintillators with fast timing response can be found at various positions of the R³B setup. The ToFD detector, located behind the dipole magnet at the end of the evacuated beam line for fragments, measures the time-of-flight (t_{flight}) and the nuclear charge (Z) of heavy fragments after the reaction in the target. The nuclear charge of reaction products is obtained by precise energy-loss measurements (ΔE) of the fragments passing through the scintillator material. The new detector should be able to separate the nuclear charge Z from $Z-1$ even for the heaviest fragments. In case of Pb fragments, a relative nuclear-charge precision σ_Z/Z of better than 0.4% is required to separate Z from $Z-$

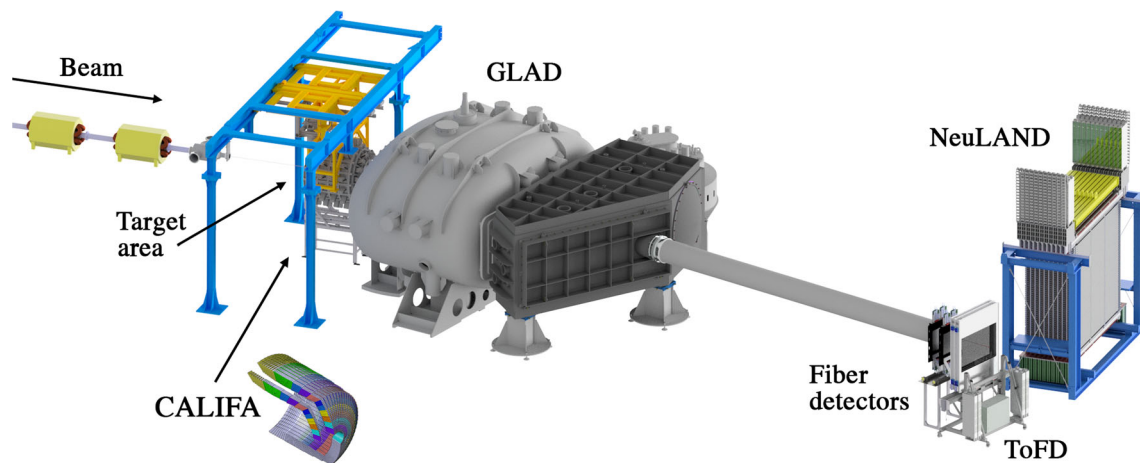


Fig. 1 R³B experimental setup: The ion beam enters from the left and hits a solid target or a liquid-hydrogen target in the target area. The target is surrounded by CALIFA, a gamma spectrometer and target recoil calorimeter. After a reaction in the target, the fragments are deflected by

the magnetic field of GLAD. Fiber detectors behind the magnet record the position of the fragment track. The ToFD detector measures the time-of-flight and the energy loss of the ions. Neutrons from reactions are unaffected by the GLAD magnet and hit NeuLAND

¹. This translates into an energy-loss measurement with a relative precision $\sigma_{\Delta E}/\Delta E$ better than 1%.

Another requirement on the performance of the new ToFD detector comes from the identification of residues in mass. The mass-over-charge ratio of the fragment can be calculated from the measured time-of-flight and the measured trajectory through the dipole field according to the following equation:

$$\frac{A}{Z} = \frac{e}{m_0 c} \cdot \frac{B\rho}{\beta\gamma}, \quad (1)$$

where A is the mass number, Z is the charge of the nucleus, e is the electron charge, m_0 is the atomic mass unit, c is the speed of light, $B\rho$ is the magnetic rigidity, β is the velocity relative to the speed of light, and γ is the corresponding Lorentz factor.

Once the nuclear charge Z is obtained from energy-loss measurements, the relative uncertainty in the mass determination can be calculated as:

$$\frac{\sigma_A}{A} \approx \frac{\sigma_{B\rho}}{B\rho} + \gamma^2 \cdot \left(\frac{\sigma_{t_{\text{flight}}}}{t_{\text{flight}}} + \frac{\sigma_L}{L} \right), \quad (2)$$

where t_{flight} is the time-of-flight between the start detector and the ToFD detector, and L corresponds to the flight path. Also here, the strongest constraint comes from the identification of the heaviest residues in the lead-uranium region, where the relative difference in mass between two neighbouring nuclei amounts to $\sim 0.5\%$. In order to resolve the masses¹, the relative uncertainty in mass must be of the order $\sigma_A/A < 2 \cdot 10^{-3}$. This would also match the uncertainty of the magnetic rigidity of about 10^{-3} that can be obtained via particle tracking.

¹ Assuming a gaussian shape for the distribution of a single fragment, a distance between two neighbouring peaks should be larger than the FWHM of the single peak in order to separate them.

Table 1 Required time-of-flight precision for several different cases to fulfill $\sigma_A/A < 2 \cdot 10^{-3}$, assuming a flight path of 20 m

Beam	Energy (GeV/nucleon)	$\sigma_{t_{\text{flight}}}/t_{\text{flight}}$ (%)	$\sigma_{t_{\text{flight}}}$ (ps)
¹² C	0.5	1.456	1280
⁵⁸ Ni	0.5	0.267	235
¹³² Sn	0.5	0.093	82
²⁰⁸ Pb	0.5	0.044	38
²³⁸ U	0.5	0.033	29
¹² C	1.0	0.799	609
⁵⁸ Ni	1.0	0.146	112
¹³² Sn	1.0	0.051	39
²⁰⁸ Pb	1.0	0.024	18
²³⁸ U	1.0	0.018	14

For typical beam energies of 1 GeV/nucleon ($\gamma \sim 2$), the time-of-flight of the heaviest residues has to be measured with a relative uncertainty of less than $2 \cdot 10^{-4}$ (sigma) in order to obtain the desired mass resolution. Considering a flight path of ~ 20 m, this results in an ultimate time-of-flight precision better than 14 ps for nuclei in the lead-uranium region at 1 GeV/nucleon kinetic energy. For several other cases the required time-of-flight precision (assuming a 20 m flight path) is given in Table 1.

Furthermore, since the unreacted beam also hits the ToFD detector, it must be able to maintain its performance even at high beam rates of up to $1 \cdot 10^6$ particle/s, and the associated electronics must have multi-hit capabilities. Here, it is important to note, that not only the energy- and time-precision have to remain stable at different counting rates, but also the mean

positions of measured energy-loss and time signals must not shift with counting rate. If, for example, at different rates the measured energy-loss signal shifts in its position by more than 1%, this could lead to wrong nuclear-charge identification.

The final detector, designed to fulfill the specifications mentioned above, consists of four planes of scintillators, and has an active area of about $1200 \times 100 \text{ mm}^2$. Each plane contains 44 vertical scintillator bars; each bar has the dimensions $27 \times 1000 \times 5 \text{ mm}^3$. The scintillator bars are read out by Photo-Multiplier Tubes (PMTs) on both far ends. The width of a single bar is matched to the size of a PMT, in order to completely omit light guides, and couple the scintillator bars directly to the PMTs, thus maximizing the light collection. To use the detector at high counting rates, it is required (see Sect. 4.2) that the PMTs are equipped with fully active voltage dividers, and that the signals delivered by the detector are adjusted to a voltage region where the PMTs have the best performance with regard to rate stability and nuclear-charge resolution. Thus, associated read-out electronics must be able to work with small currents from the PMTs.

To design the detector, we have performed simulations of the time resolution to investigate the influence of different components on the detector resolution, and to choose appropriate scintillator material and PMTs, see Sect. 3. We carried out different measurements with a prototype detector using LEDs, laser, and relativistic heavy ion beams to test timing and the quality of energy-loss measurements, see Sect. 4.

3 Simulations

GEANT4 [10] simulations with optical photons were performed to model the timing response of the detector and to evaluate the contribution of the various processes that determine the timing precision. However, simulations with photon tracking are computationally intense and, therefore, calculations using the statistical model (see below) were also performed. The statistical model is presented first as it captures the main factors affecting the time resolution in scintillators.

3.1 Time precision using the statistical model

The statistical model as originally described in Ref. [11] was used to study different effects influencing the time precision and search for a compromise between best-performance capabilities and costs. Several statistical processes limit the attainable time precision of scintillation detectors, such as:

- time spread in the energy transfer to the optical levels of the scintillation,
- decay time of the excited states,

- fluctuations in the propagation time of photons through the scintillator,
- creation of photo-electrons within the photo cathode of the photomultiplier, and
- the associated electronics.

First studies on the statistical limitations on the achievable time precision using scintillation detectors have been done in the early 1950s by Post and Schiff [11]. The basic idea of their model is that the probability $P_M(t)$ that M photomultiplier pulses occur between the time zero (defined as the time of the initial excitation of the scintillator), and the time t is given by the Poisson distribution:

$$P_M(t) = \frac{1}{M!} \cdot [N(t)]^M \cdot \exp[-N(t)], \quad (3)$$

where $N(t)$ is the average expected number of photomultiplier pulses in the range $[0, t]$, with $R_{\text{tot}} = \int_0^\infty N(t) dt$ being the average total number of created photoelectrons. Starting from this probability distribution, the probability that the Q^{th} photoelectron is detected in the time interval $[t, t + dt]$ can be calculated as [11]:

$$W_Q(t) = P_{Q-1}(t) \cdot \frac{dN(t)}{dt} \\ = \frac{1}{(Q-1)!} \cdot [N(t)]^{Q-1} \cdot \exp[-N(t)] \cdot \frac{dN(t)}{dt}. \quad (4)$$

The time precision σ_t can then be calculated from the variance of the time signal:

$$\sigma_t^2 = \langle t^2 \rangle - \langle t \rangle^2 = \frac{1}{W_Q^{\text{tot}}} \cdot \int_0^t t^2 \cdot W_Q(t) dt \\ - \left(\int_0^t t \cdot W_Q(t) dt \right)^2, \quad (5)$$

where W_Q^{tot} is the total probability that the Q^{th} photoelectron occurs in the range $[0, \infty]$ and is given as [11]:

$$W_Q^{\text{tot}} = 1 - \exp \left(-R_{\text{tot}} \cdot \sum_{i=1}^Q \frac{R_{\text{tot}}^{i-1}}{(i-1)!} \right). \quad (6)$$

As a result of this approach, the limiting factors obtained for the time precision are the average total number of photoelectrons R_{tot} ($\sigma_t \sim 1/R_{\text{tot}}^{1/2}$) as well as the involved scintillator decay timing constants. Based on these ideas, many different studies dedicated to the timing properties of scintillator detectors have been performed [13–23].

Usually, the function $dN(t)/dt$ is given as a convolution of the different above-mentioned contributions influencing the time precision. On the other hand, as these processes (photon

production and photon transport, photoelectron conversion, and signal processing) are statistically independent, one can calculate the timing precision for each of them (σ_i) using above equations, and then obtain the total time precision as a quadratic sum of individual components, i.e. $\sigma_t^2 = \sum \sigma_i^2$. This allows to separately study and optimize the influence of different contributions from scintillator, photomultiplier, and electronics to the timing precision.

The intrinsic² contribution of a scintillation detector to the overall time precision is determined by the time-distribution of the produced light signal and by the amount of produced light. In case of a plastic scintillator, it has been shown [24–27] that the best-suited distribution shape for the produced light signal $dN(t)/dt$ is given by a convolution of an exponential and a Gaussian function:

$$\frac{dN(t)}{dt} \sim f_G(t) * \exp(-t/\tau),$$

$$f_G(t) = \frac{1}{\sigma \cdot \sqrt{2\pi} \cdot \exp\left(-\frac{(t-3\sigma)^2}{2\sigma^2}\right)}, \quad (7)$$

where $\sigma = \tau_{\text{rise}}/\ln(9)$ and $\tau = \tau_{\text{decay}}$, with τ_{rise} and τ_{decay} being, respectively, rise and decay times of a given scintillator material as given by the supplier.

Concerning the use of Eq. 7, as the involved functions are Gaussian and exponential, time-consuming numerical convolutions are not necessary. A convoluted function is known as exponentially modified Gaussian function (*ExGaussian*) and can be easily calculated as [28]:

$$\frac{dN(t)}{dt} = \frac{1}{2 \cdot \tau} \cdot \exp\left(\frac{\sigma^2}{2 \cdot \tau^2} - \frac{t - 3 \cdot \sigma}{\tau}\right) \left[1 - \operatorname{erf}\left(\frac{\sigma}{\sqrt{2} \cdot \tau} - \frac{t - 3 \cdot \sigma}{\sqrt{2} \cdot \sigma}\right)\right]. \quad (8)$$

To calculate the intrinsic resolution of a scintillation detector, we see from Eqs. 4 and 5 that apart from the light-pulse shape $dN(t)/dt$ the average expected number $N(t)$ of light pulses in the range $[0, t]$ is also required. For an *ExGaussian* function one would obtain:

$$N(t) = R_{\text{tot}} \cdot \frac{f(t) - f(0)}{0.5 - f(0)},$$

$$f(x) = 0.5 \cdot \left\{ \operatorname{erf}\left(\frac{x - 3 \cdot \sigma}{\sqrt{2} \cdot \sigma}\right) - \exp\left(\frac{\sigma^2}{2 \cdot \tau^2} - \frac{x - 3 \cdot \sigma}{\tau}\right) \left[1 + \operatorname{erf}\left(\frac{x - 3 \cdot \sigma}{\sqrt{2} \cdot \sigma} - \frac{\sigma}{\sqrt{2} \cdot \tau}\right)\right] \right\}. \quad (9)$$

² Under intrinsic contribution we assume only contributions to the time precision coming from the light production. No light transport is considered at this stage.

For small-size (a few cm) scintillation detectors, the light-production mechanism described above plays the dominant role. For timing properties of larger-size detectors, light transport becomes more important, see e.g. Ref. [12] and references therein. In this case, the light pulse which arrives at the photomultiplier, $dN_{\text{SCI}}(t)/dt$, can be considered as a convolution of two contributions due to light-production processes, $dN_{\text{LP}}(t)/dt$, and from the light-transport processes, $dN_{\text{LT}}(t)/dt$:

$$\frac{dN_{\text{SCI}}(t)}{dt} = \frac{dN_{\text{LP}}(t)}{dt} * \frac{dN_{\text{LT}}(t)}{dt}, \quad (10)$$

where $dN_{\text{LP}}(t)/dt$ is given by Eq. 8.

To calculate the contribution from the light transport, we have followed the work of Ref. [12]. We assume, for simplicity, that photons created in the interaction between a traversing particle and the scintillation material are coming from a point-like source positioned at a distance L from the end face of a scintillator which is coupled to a PMT. Assuming an isotropic distribution of created photons, we obtain that $dN_{\text{LT}}/dt = -2 \cdot \pi \cdot L \cdot n_{\text{sci}}/(c \cdot t^2)$, with n_{sci} being the refractive index of the scintillation material, and c the velocity of light in vacuum. It is important to note that absorption processes of photons (L_{att} being the attenuation length) during their transport also influence the propagation-time distribution. Taking this effect into account, we can write for $dN_{\text{LT}}(t)/dt$:

$$\frac{dN_{\text{LT}}(t)}{dt} = -2 \cdot \pi \cdot \frac{L \cdot n_{\text{sci}}}{c \cdot t^2} \cdot \exp\left(-\frac{c \cdot t}{n_{\text{sci}} \cdot L_{\text{att}}}\right). \quad (11)$$

The above function is non-zero only for propagation times between minimum propagation time t_{min} and maximum propagation time t_{max} . If we neglect scattering processes of photons on the surface of the scintillator, we can obtain a direct correlation between the propagation time t of a given photon and its initial axial angle θ :

$$t = \frac{L \cdot n_{\text{sci}}}{c \cdot \cos \theta}. \quad (12)$$

The minimum propagation time t_{min} is obtained for a direct photon trajectory, i.e. for $\theta = 0$: $t_{\text{min}} = L \cdot n_{\text{sci}}/c$, and the maximum t_{max} propagation time is given by a maximum axial angle for which the photons are still reflected in the direction of a photomultiplier: $t_{\text{max}} = L \cdot n_{\text{sci}}/(c \cdot \cos \theta_{\text{max}})$. As a good approximation we can calculate θ_{max} as $\theta_{\text{max}} = \pi/2 - \theta_{\text{tot_refl}}$, where $\theta_{\text{tot_refl}}$ is the critical angle for total reflection.

Knowing the light-pulse shape seen by a PMT (see Eq. 10) and using the statistical model, one can calculate the contribution of the scintillator σ_{sci} . The contribution from the PMT is determined by its transient-time-spread (t_{tts}) and is calculated as: $\sigma_{\text{PMT}} = t_{\text{tts}}/(2.35 \cdot \sqrt{R_{\text{tot}}})$. Then, the total time precision σ_t becomes: $\sigma_t = \sqrt{\sigma_{\text{sci}}^2 + \sigma_{\text{PMT}}^2 + \sigma_{\text{el}}^2}$, where σ_{el} is the contribution from electronics. For simplicity, we assume

Table 2 Characteristics of considered scintillation materials from Eljen Technology [31]

Parameter	EJ200	EJ204	EJ232
Rise time (ns)	0.9	0.7	0.35
Decay time (ns)	2.1	1.8	1.6
Attenuation length (cm)	210	140	17
Light output (% Anthracene)	64	68	55
Scintillation efficiency (photons/1 MeV e ⁻¹)	10,000	10,400	8400
Wavelength of max emission (nm)	425	408	370
Ratio H:C atoms	1.102	1.100	1.101
Density (g/cm ³)	1.023	1.023	1.02
Refractive index	1.58	1.58	1.58

that the traversing particle is passing through the centre of a bar. We have taken numerical values of R_{tot} that correspond to the number of photoelectrons created due to passage of relativistic 1 GeV/nucleon ions ranging from ^{12}C to ^{238}U through the given thickness and type of scintillation material. To do this, we have calculated the energy loss of the passing ions using the ATIMA code [29], with the number of electrons per MeV deposited energy as given by the scintillator supplier, calculated the quenching factor suited for heavy-ion beams at relativistic energies according to Ref. [30], with the geometrical efficiency from GEANT simulations (see below), and considered the quantum efficiency of a given photomultiplier as provided by the supplier.

For calculations presented here, we have assumed three different scintillation materials: EJ200, EJ204 and EJ232 from Eljen Technology [31], see Table 2; very similar properties are also reported for BC408, BC404 and BC422, respectively, from Bicron. We have considered only these three materials, as these are all characterized by short rise and decay times. These are mandatory conditions to reach excellent time precision and to operate in high count-rate experiments. The R8619-20 photomultiplier from Hamamatsu was chosen for the ToFD and thus used in these calculations. For the contribution of electronics σ_{el} , for a single read-out channel a value of 13 ps is assumed. This is a typical electronic single-channel time-precision of a FQT-TAMEX3 board, which is chosen for the final detector, see Sect. 4.1.

Table 3 presents the time precision required to separate A from $A - 1$ in different mass regions. In the same table, also shown is the achievable time precision of the new ToFD detector calculated using the statistical model described above. Due to the higher deposited energy, and thus higher light production, the calculated time precision improves with increasing nuclear charge of the considered fragment. For all three scintillation materials, the calculated

Table 3 For each considered fragment, the time precision required $\sigma_t^{\text{required}}$ to separate A and $A - 1$ in the R³B setup is shown. Also results of simulations for three different scintillator-material types are included (columns 3–5). A 1 GeV/nucleon kinetic energy and a flight path of 20 m is assumed

Fragment	$\sigma_t^{\text{required}}$ (ps)	σ_t (ps) EJ200	σ_t (ps) EJ204	σ_t (ps) EJ232
^{12}C	609	32	27	14
^{58}Ni	112	16	14	8.9
^{132}Sn	39	10	9.8	7.0
^{208}Pb	18	7.8	7.3	5.8
^{238}U	14	7.3	8.8	5.7

time precision is better than the design goals. The best precision, especially for light nuclei, is achieved with EJ232. Nevertheless, due to the porosity of EJ232, it is not possible to produce bars of the size required for the ToFD detector, and it was therefore excluded from further consideration.

For the EJ200 and EJ204 scintillation materials, Fig. 2 shows the different contributions to the total time precision of the new ToFD detector assuming a ^{208}Pb beam at 1 GeV/nucleon.

The contribution of the photomultiplier to the time precision is negligible, due to the high amount of photons produced after the passage of relativistic heavy ions through the detector. Thus, there is no need to use very fast and expensive photomultipliers in order to obtain the required time precision.

The contribution of the electronics for the whole detector is about 5 ps. Such a good electronic resolution can be achieved using a FQT-TAMEX3 board [44] developed in the EE department at GSI, see Sect. 4.1. Please note, that each of the four layers of bars measures the time-of-flight, and hence, we obtain a better electronic resolution for the whole detector than for one channel.

The contribution from the light production and light transport in the scintillator material to the total time precision is of the same order as the contribution from the electronics.

3.2 GEANT4 simulations

The geometry of the individual scintillators as well as the full detector assembly was studied using the GEANT4 simulation toolkit [32] including the package for optical photon tracking. The simulations included light production by fragments traversing the scintillators, tracking of the photons to the PMTs at the far ends of the scintillators, quantum efficiency of the photo-cathode, convolution with the single-electron response of the PMT, and leading-edge timing at a given threshold.

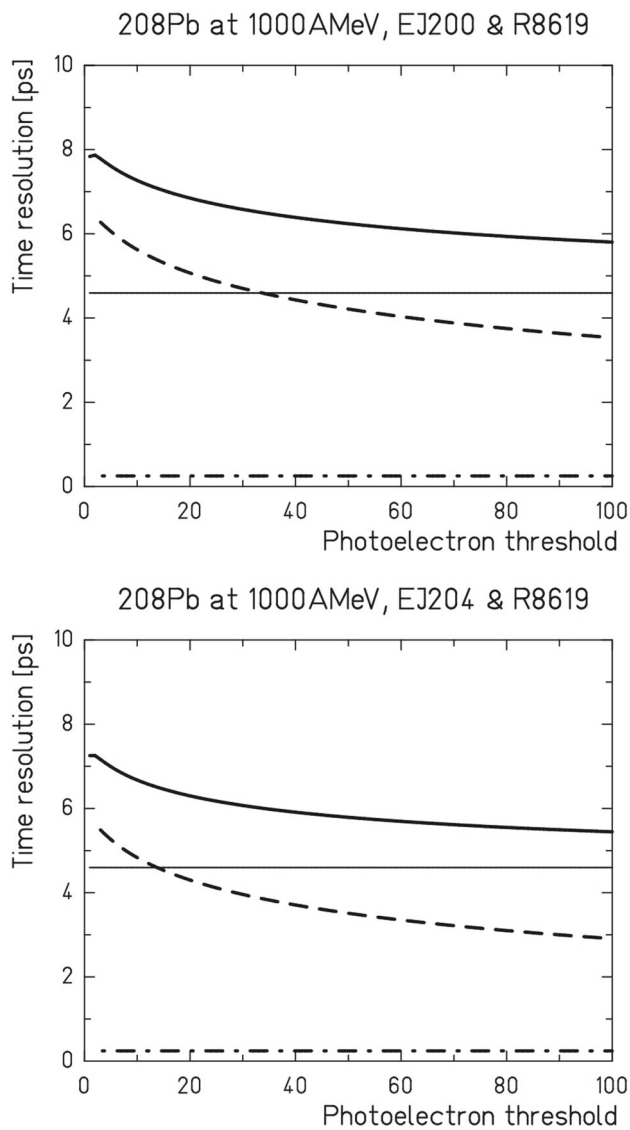


Fig. 2 Different contributions to the total time precision of the new ToFD detector calculated for ^{208}Pb at 1 GeV/nucleon assuming EJ200 (top) or EJ204 (bottom) scintillation material: Photomultiplier (dash-dotted line), electronics (thin full line), scintillator (dashed line), and total (thick full line)

For the production of the scintillation light in GEANT4 the bi-exponential function is used:

$$I_t = \frac{I_0}{\tau_{\text{decay}} - \tau_{\text{rise}}} (\exp[-t/\tau_{\text{decay}}] - \exp[-t/\tau_{\text{rise}}]), \quad (13)$$

where I_0 is the photon yield, and τ_{rise} and τ_{decay} are the rise and decay times of the scintillator material. Please note, that the bi-exponential function given above, which is used in GEANT4, is well-suited for a liquid scintillator, but not for the shape of a light pulse from a plastic scintillator [24–27].

One of the most important ingredients to calculate the expected timing precision is the number of photons produced by the impinging ion. The energy loss can be calculated rather

accurately, but the light output is quenched and depends on the ionization density. The calculation of the quenching factor produces one of the largest systematic uncertainties in the prediction of the time precision.

In GEANT4, Birk's formula is implemented in order to calculate the photon yield dL/dx as a function of the energy loss per path length dE/dx :

$$\frac{dL}{dx} = L_0 \cdot \frac{dE/dx}{1 + k_B \cdot dE/dx}. \quad (14)$$

k_B is Birk's constant and the proposed value for polystyrene-based scintillators is 0.126 mm/MeV (see also Ref. [33]). With this value, GEANT4 predicts that about 400,000 photons are produced for each incoming Ni fragment. However, if one compares this with the results of the statistical model calculation where Ref. [30] was used to calculate the quenching factor, the GEANT4 value is smaller. It should be noted that the quenching factor calculated with Birk's law in Ref. [33] is used for minimum-ionizing particles and Ref. [30] is more suited for heavy ions. Therefore, we adapted a value for Birk's constant which produces for the Ni beam the same amount of photons as in the statistical model. In Sect. 6, these values are also compared to measurements.

In the simulations, the scintillator bar is read out at both ends by PMTs with a diameter of 25 mm, and photons were then tracked until they reached the corresponding PMT. The arrival-time distribution of photons is shown in the top part of Fig. 3.

In the next step, the quantum efficiency of 28% of the photo-cathode was taken into account and the t_{tts} of the PMT was simulated by adding a transit time, which followed a truncated Gaussian distribution with the corresponding width given by the PMT's properties. In addition, the single-electron response (SER) of a PMT was recorded and digitized. In this way, an electronic pulse (see Fig. 3 bottom) could be reconstructed by adding the SER at each time a photo-electron was registered in the simulations. A comparison between the top and bottom parts of Fig. 3 shows clearly the influence of the PMT. The rise time of the signal gets longer and the width larger. Using the time when the signal was above a given threshold, a leading-edge discriminator is simulated.

By plotting the arrival-time distributions of the n^{th} electron for many events (see Fig. 4), we can obtain the expected time precision as the spread (sigma) of the distribution.

In this way, simulations for a 500 MeV/nucleon Ni beam impinging on a scintillator with dimensions $27 \times 800 \times 5 \text{ mm}^3$ have been performed. These simulations can be directly compared to the measurement performed during the GSI S438 beam time in 2014.

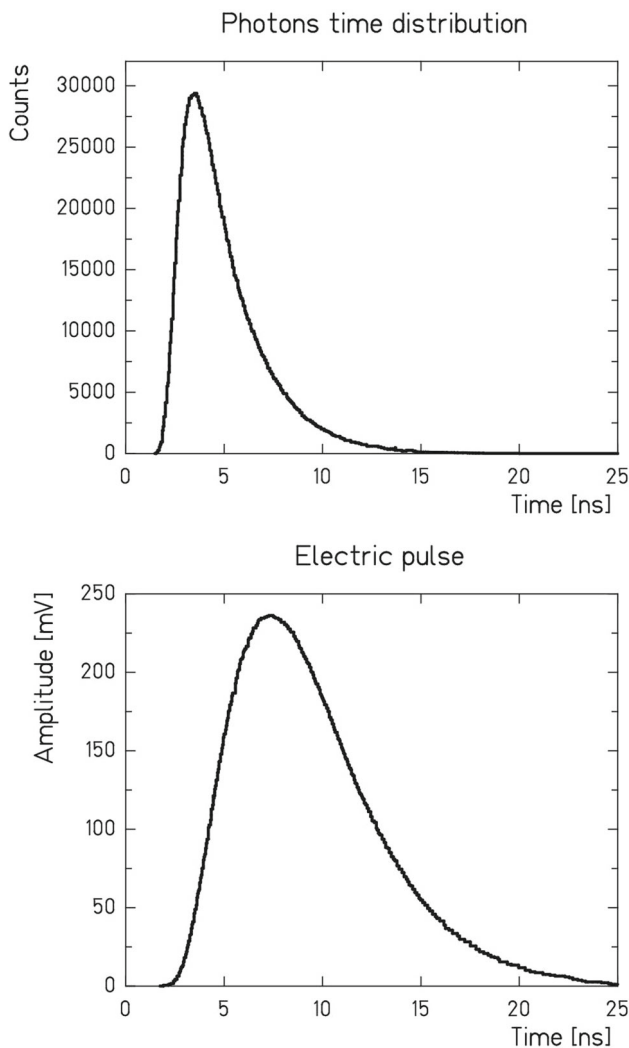


Fig. 3 Arrival-time distribution of the photons at the PMT (top) and the resulting electric pulse (bottom)

3.3 Comparison between GEANT4 simulations and statistical model

The predictions of the statistical model and GEANT4 simulations for the time precision of the ToFD detector are shown in Fig. 5. In both cases the same experimental conditions were assumed that were met during the S438 beam time: ^{58}Ni beam at 500 MeV/nucleon kinetic energy impinging on the detector made out of EJ204 scintillation material. For the contribution from each single electronic channel 25 ps was used as it was measured during the experiment with the test electronics.

The agreement between these two sets of calculations is rather good. In both cases, the strongest contribution comes from the electronics. As already mentioned, using the FQT-TAMEX3 read-out for the final detector, we are able to reduce the contribution from the electronics by a factor of two compared to the old electronics. The contributions from the scin-

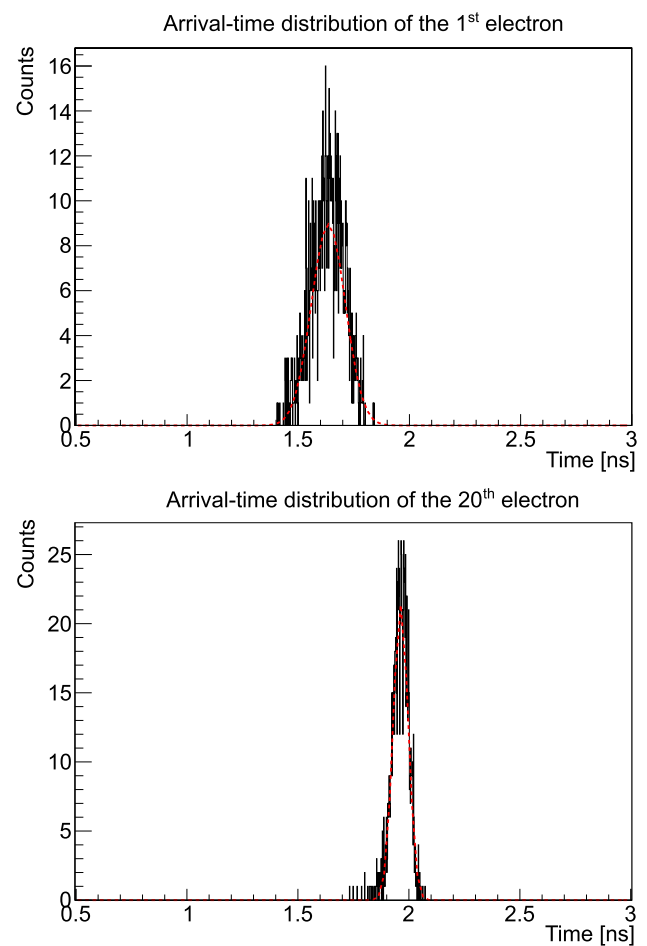


Fig. 4 Examples of arrival-time distribution of the 1st (top) and the 20th (bottom) photo-electron. The spread of the distribution yields the achievable time precision

tillation material - light production and light transport are also rather similar in both cases. Although the two sets of simulations use different shapes for the light pulses, due to the large amount of produced photons, details of the light-pulse shape do not have a strong influence. Somewhat different are the predictions for the contribution of the photomultiplier which in the statistical model is smaller than in the GEANT4 simulation. This can be explained, as in the GEANT4 simulations details of the single-electron response of the photomultiplier have been considered, which was not the case in the statistical model, see Sect. 3.1. Nevertheless, both models show that the design goals concerning timing precision with the new ToFD detector can be fulfilled with the particular combination of components and design parameters.

4 Prototype developments and results

Energy and time precision of the ToFD detector have been studied using a fast LED, a picosecond pulsed diode laser and several different heavy-ion beams at relativistic energies.

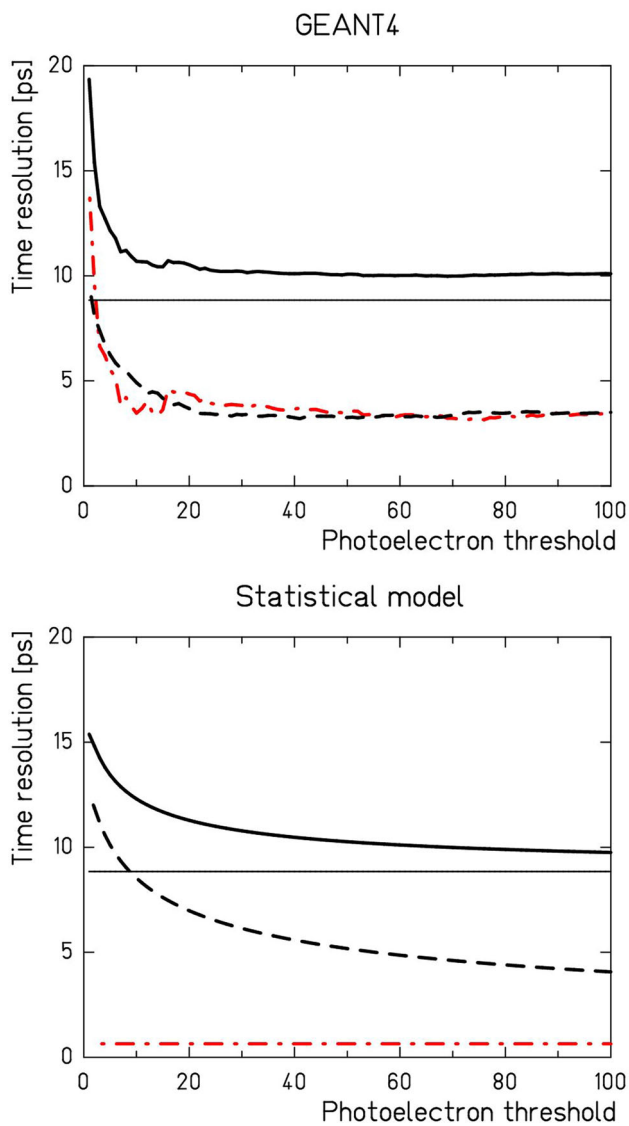


Fig. 5 Time precision of the new ToFD detector calculated with GEANT4 (top) and the statistical model (bottom) assuming a ^{58}Ni beam at 500 MeV/nucleon. Shown are different contributions to the total time precision (full thick line): electronics (thin full line), photomultiplier (dashed-dotted line), light production and light transport (dashed line)

The prototype detector consisted of 4 layers. Each layer was composed of 6 bars with a length of 800 mm and a width of 27 mm, but those in the first two layers had a thickness of 3 mm, and those in the last two layers a thickness of 5 mm (see Fig. 6). The bars were made of scintillation material EJ204 and were read out at both ends with the R8619-20 PMTs from Hamamatsu. Tests performed with a fast LED have shown (see below) that these PMTs are best suited for our purposes.

4.1 Readout electronics

To fulfill the design goals of the new ToFD detector, appropriate read-out electronics had to be developed. The electronics

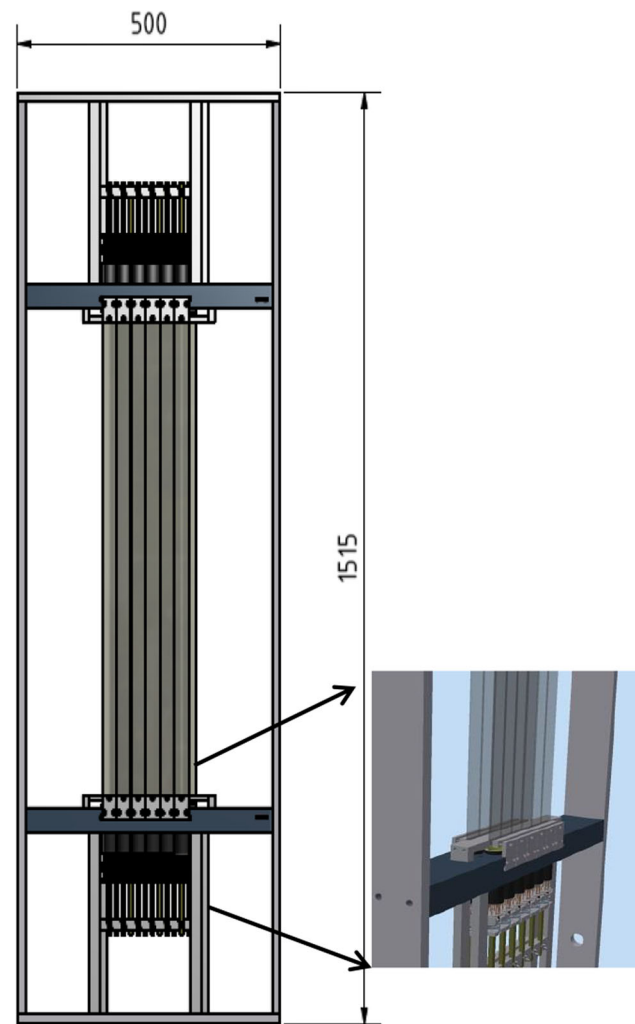


Fig. 6 Schematic view of the ToFD prototype detector used in the test experiment. On the left part of the figure the front view of the prototype is shown. The inset on the right shows holding structures for scintillator bars and photomultipliers

need to measure the time and the charge of the PMT pulse with sufficient precision. And, as already discussed above, in order to cope with high-counting rates, new read-out electronics has to have multi-hit capability. The final electronics consists of a front-end board called FQT and a FPGA-based TDC with the name TAMEX3. It is described in detail in this Section. However, many results with prototype detectors shown in this paper were achieved with other electronics. Therefore, we describe in this Section the used electronics in chronological order.

When starting on the R&D for a new ToFD detector, a read-out system based on the general purpose Pre-Amplifier-Discriminator (PADI [43]) together with VFTX modules [35] were available. For the signal shape produced by the ToFD detector, a time precision of about 15 ps per channel can be expected with the PADI system, while the charge is measured

by a Time-over-Threshold (ToT) method. In a ToT approach [41], the input signal is compared to a pre-defined threshold value in order to convert collected charge to a digital time signal with a width corresponding to the input charge. A disadvantage of the standard ToT method is the non-linearity between the collected charge and the width of the digitized signal [42] which in our case would result in large difficulties to identify and separate heavy fragments in the lead-uranium region in nuclear charge.

To overcome this problem, a new development based on the TacQuila board, developed originally for the FOPI experiment [37,38], was initiated. TacQuila is based on a high resolution Time-to-Amplitude Converter ASIC chip for time measurement, and has compact read-out functionality. A time precision of up to ~ 10 ps per channel [34] can be achieved using this board. The TacQuila board runs in a free common-stop mode relative to an external clock. TacQuila-based read-out comprises also a 16-channel Front-End Electronics (FEE) board for signal amplification, splitting and discrimination [39]. Additionally, a control board TRIPLEX [40] offers individual thresholds for each channel, a multiplicity signal, an analogue sum, an 'OR' signal, a pulser to trigger the timing branch and a multiplexer. Charge is measured via a Charge-to-Time-Digital-Converter (QTC) board - the input charge signal is shaped and integrated, as in the case of the QTC board, and the signal integration enables a linear charge measurement. The Time-over-Threshold of the integrated signal is then taken as a measure of the deposited energy and for nuclear-charge identification. This overcomes the problem with the non-linearity of the ToT method discussed above.

For the purpose of the R^3B experiments, on the basis of the TacQuila board, a new front-end electronic board named FQT (Front-End, charge Q and Time) has been developed, and the new version of the system is also adopted for the ToFD detector. The new multichannel electronic card, called FQT-TAMEx3 system [44], is a combination of the new FEE board FQT and an FPGA-based TDC from the VFTX module [36]. The time precision is 13 ps per channel, and the module is multi-hit capable. The FQT board combines the QTC board, the control board TRIPLEX, and the FEE board all in one PCB, whereas for the TacQuila readout these were all on separate boards. Combining several boards into just one reduces the number of required PCBs and the required space, as well as the price per channel.

In the FQT board, the incoming signals are shaped and integrated, thus providing the linearity required for the charge measurement. Tests performed with the new card have shown that the linearity of the charge measurements persists over a large range of PMT signal amplitudes [45]. Digital time signals produced by the FQT board are sent to a TAMEx3 card to determine their leading and trailing edges. The time measurement is split into a fine and a coarse measurement, corresponding to a time relative to the next clock cycle and



Fig. 7 New multi-channel electronic card FQT-TAMEx3. The card consists of two boards which are plugged together via a multi-pin connector. The board on the right is the front-end-electronics FQT and on the left one can see the FPGA-TDC Tamex

the number of the clock cycles, respectively. The Time-over-Threshold is then obtained as a difference between trailing and leading times of the integrated signal, and is used in the data analysis as a measure of the energy deposited in the detector by traversing particles. The system also includes a backplane, which enables connections to the low-voltage power supply as well as to an optical link for communication and data transfer. The FQT-TAMEx3 is used for the final detector.

At the time the detector prototype was tested, this electronic card was still under development. Thus, for the prototype testing we have used the PADI-VFTX combination, as well as a prototype of a TAMEx board combined with the LAND front-end [34]. As the TAMEx prototype did not have a QTC included, for several tests with LED we have also used a separate QTC module IWATSU CLC101 [46] combined with the VFTX module. This setup was only used for tests on measurements of the precision in the energy deposit, as the IWATSU CLC101 module has a time precision of the order of 100 ps, and thus is not suitable for our timing measurements.

4.2 Energy precision of the prototype detector

The energy precision of a prototype of the new ToFD detector was investigated using a test stand with a fast LED, a test stand with laser and also during the GSI beam time in April 2014 (experiment S438). These tests had several measurement goals: Testing the influence of the photomultiplier's properties on the energy-loss resolution at different counting rates, testing the position-dependence of the measured energy-loss signal, and testing the nuclear-charge resolution for different relativistic beams. The goal of these tests was

to find conditions enabling energy resolution of better than 1%, stable over different counting rates in the range 1 kHz–1 MHz.

4.2.1 Photomultiplier choice

Due to the large number (352) of read-out channels, the photomultiplier to be used for the new ToFD detector has to be cost-effective, its diameter should match the width of the bars to obviate any light guides, and in order for the detector to be used in high count-rate experiments it must have a stable gain. The last point implies that the PMT power-supply circuit must have a fully active voltage divider. An active voltage divider ensures that in case of large currents the voltages at the last dynodes, and consequently the gain of the PMTs are kept constant. Without an active voltage divider, the gain of the PMT varies, see e.g. Figure 12.15 in Ref. [47], and thus the peak position in the energy spectrum is strongly dependent on the counting rate. This results in a reduced nuclear-charge resolution for varying beam rates or, in the worst case, no resolution at high rates at all. Another advantage of using a photomultiplier with an active voltage divider is the decreased power consumption.

For the purposes of the NeuLAND detector, Hamamatsu has equipped the R8619 photomultiplier (see Table 4 for its properties) [48] with a fully active base following the work of Kalinnikov et al. [49]. The original version R8619 has only a partly active base (with a capacitor connected to the last three dynodes). The modified version is called R8619-20, and is also used for the new ToFD detector. The photomultiplier is directly glued to the scintillator bar using a silicone glue without any light guides.

The photomultiplier and its influence on the energy precision of a new ToFD detector have been tested using a test stand [50] with a fast LED. The type of LED used in these tests was Osram LB Q39E [51]; it emits blue light with 420 nm wavelength. To obtain realistic conditions, the LED was pulsed in random mode using the programmable pulse generator LeCroy 9210 with external trigger [52]. With this pulse generator, signals of different shapes at different rates can be generated. For comparison, we also studied the original version R8619.

The pulse frequency of the LED was varied between 5 and 800 kHz³. The analog outputs of the PMTs were sent directly to a charge-to-time converter QTC module IWATSU CLC101 [46] where they were shaped and integrated. These signals were then recorded by the FPGA TDC VFTX2 [53] developed at GSI. The voltage of the PMTs was varied in order to extract different charges. The charge resolution, σ_Q , and shifts of the mean value in the charge spectrum have been

Table 4 Characteristics of the Hamamatsu R8619-20 photomultiplier [48]

Parameter	R8619
Diameter (inch)	1
Spectral response (nm)	300–650
Quantum efficiency	27%
Dynode stages	10
Anode pulse rise-time (ns)	2.5
Electron transit time (ns)	28
Transit-time spread TTS (ns)	1.2

recorded at different rates. The results of the test with LED are presented in Figs. 8 and 9.

The relative charge resolution (σ_Q/Q) measured with the two photomultipliers at different rates is shown in Fig. 8. While at low extracted-charges both PMTs give very similar results, for larger charges only the R8619-20 PMT with a fully active divider guarantees a stable resolution even for the highest counting rates.

Similar behaviour is seen in Fig. 9, where the shift in the peak position relative to the 5 kHz case as a function of the counting rate is shown for three different values of extracted PMT charges. For the photomultiplier with a fully active base, the shift in the mean charge with increasing rate is smaller than in the case of a PMT with a partly active base. We can see, that for smaller extracted charges, the relative shift in the peak position in the charge spectrum stays below 1% over the whole counting-rate range (5–800 kHz).

The stability of the energy-loss measurement at different counting rates with the new ToFD detector has also been studied with a ^{58}Ni beam at 500 MeV/nucleon during the S438 experiment at GSI. For this, the detector prototype as shown in Fig. 6 was used. In these tests, only R8619-20 PMTs were used.

Figure 10 shows nuclear charges determined using the prototype detector for the incoming ^{58}Ni beam and its reaction products. The voltage of the PMTs was set to 500 V, corresponding to a PMT signal height of about 200 mV (top left and right, and bottom left in Fig. 10) and to 400 V corresponding to 60 mV signal height (bottom right in Fig. 10). By fitting the main peak we obtain a nuclear-charge resolution of $\sigma_Z = 0.19$ charge units (for $Z = 28$) at the lowest rate of 5 kHz, which corresponds to $\sigma_Z/Z = 0.68\%$. Even at the highest rate of 1000 kHz an excellent relative nuclear-charge resolution of 0.84% has been obtained, which is well below the required value of 1.5% to separate Ni from Co.

A summary of all measurements with ^{58}Ni beam is shown in Table 5. Nuclear-charge resolution as well as the shift in the position of the main $Z = 28$ peak relative to the 5 kHz measurement are presented. One can see that up to about 300 kHz counting rate, the shift is about 1% or less. Only at

³ 800 kHz is the maximum frequency that can be reached with the LeCroy pulser using external trigger.

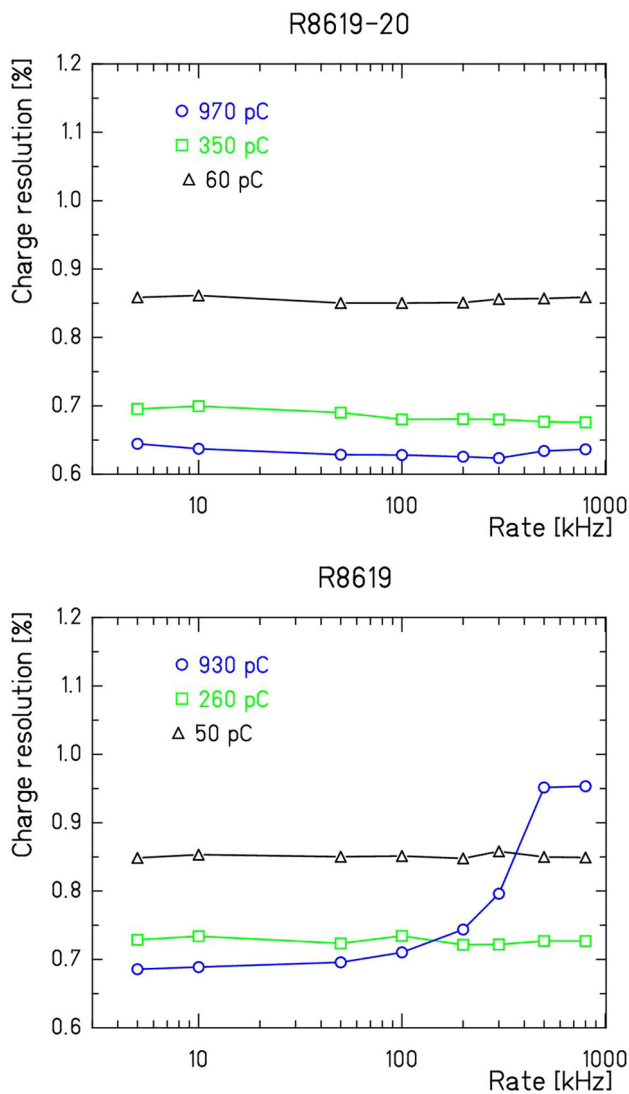


Fig. 8 Relative charge resolution (σ_Q/Q) at different rates measured using R8619 (bottom) and R8619-20 with a fully active voltage divider (top) at three different values of extracted PMT charges

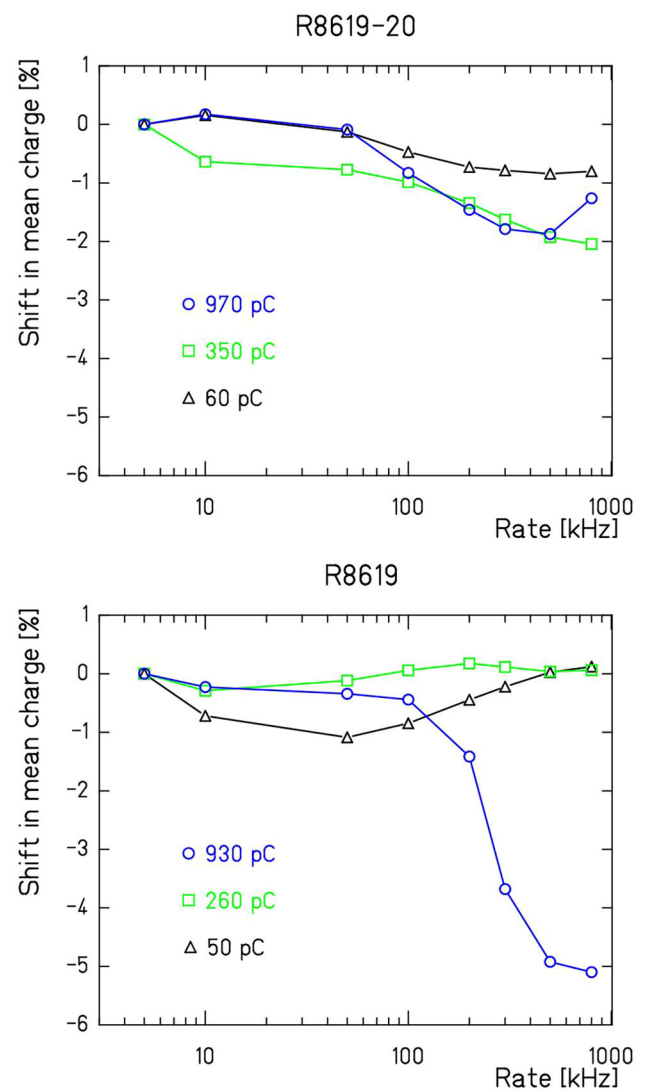


Fig. 9 Shift in the peak position in the charge spectra for different rates measured at three different values of extracted PMT's charges. Top: R8619-20 photomultiplier with active base, bottom: R8619

higher rates the shift becomes larger than 1% which is not acceptable.

The situation can be considerably improved if one performs measurements with a smaller amplitude of the PMT signals. By decreasing the HV values to 400 V, corresponding to about 60 mV PMT signal height, we reached, during the experiment, very stable nuclear-charge measurements, where the relative shift in Z remained below 1% also for the highest rates of 1000 kHz while still keeping the excellent nuclear-charge resolution, see Fig. 10 bottom right. Of course, one has to compromise in the usable dynamic range, as is clearly seen from the figure.

4.2.2 Position-dependence of the energy-loss signal of the prototype detector

Due to light attenuation along a scintillator bar, the energy E_{PMT} measured by a single PMT depends on the position of the fragment impact along the bar [54]: $E_{\text{PMT}} = E_0 \cdot \exp(-\lambda \cdot x_{\text{PMT}})$, where E_0 is the deposited energy, λ the absorption coefficient, and x_{PMT} the distance between the impact point of the fragment and the PMT. If a scintillator bar is read out at both far ends, as it is in our case, then the deposited energy E_0 can be obtained from the geometrical mean of the energies obtained by the two PMTs:

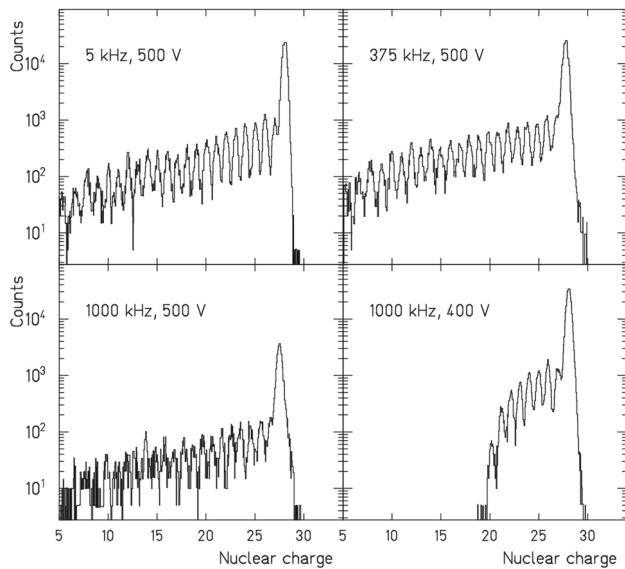


Fig. 10 Nuclear charge of the reaction products for a ^{58}Ni beam at 500 MeV/nucleon measured with the prototype of the ToFD detector at several counting rates. The spectrum is obtained from the scintillator bars read out with PADI coupled to VFTX. Top left: 5 kHz count rate; top right: 375 kHz; bottom left: 1000 kHz; bottom right: 1000 kHz and 400 V

$$\begin{aligned}
 E_{\text{geom}} &= \sqrt{E_{\text{PMT1}} \cdot E_{\text{PMT2}}} \\
 &= E_0 \cdot \sqrt{\exp(-\lambda \cdot x_{\text{PMT1}}) \cdot \exp(-\lambda \cdot x_{\text{PMT2}})} \\
 &= E_0 \cdot \exp(-\lambda \cdot L/2), \\
 \Rightarrow E_0 &= \sqrt{E_{\text{PMT1}} \cdot E_{\text{PMT2}}} \cdot \exp(\lambda \cdot L/2) \quad (15)
 \end{aligned}$$

where $L = x_{\text{PMT1}} + x_{\text{PMT2}}$ is the bar length.

Ideally, the measured energy as calculated according to Eq. 15 should be independent of the impact position of the fragment. In reality, this is not the case. Additional effects such as light refraction on the surface of the scintillator or light reflections at the ends of the scintillator have an influence on the number of photons detected by each PMT, and thus on the measured energy. As these effects depend on the impact position of the fragment, they result in position-dependence of the measured energy beyond Eq. 15. In order to obtain the required nuclear-charge resolution, one has to avoid or correct for the position-dependence of the measured deposited energy.

Firstly, we have tested the influence of different wrapping materials on the measured energy. We have performed two sets of measurements, one using a laser test-stand and one using ^{48}Ca beam at 550 MeV/nucleon kinetic energy. For the laser test-stand [55], a Picosecond pulsed Diode Laser PDL 800-D from PicoQuant GmbH [56] was used. With the driver, which is part of the laser system, it was possible to change the repetition frequency as well as the light output, thus simulating different experimental conditions. In both

Table 5 Nuclear-charge resolution measured with the ToFD prototype at different counting rates. Also shown (last column) is the shift in the position of the main peak relative to the 5 kHz run

Rate (kHz)	HV (V)	σ_Z	σ_Z/Z (%)	Shift in Z (%)
5	500	0.19	0.68	0.0
59	500	0.19	0.69	0.5
375	500	0.23	0.82	1.3
1000	500	0.23	0.84	2.4
1000	400	0.23	0.83	0.2

cases, several wrapping materials were tested: no wrapping, TYVEK [57], 3M Enhanced Specular Reflector (ESR) film [58] and standard aluminum foil.

Both sets of measurements show a strong influence of the wrapping material on the position-dependence of the deposited energy. As an example, we show in Fig. 11 results measured with a ^{48}Ca beam and with Al-foil (top), no wrapping (second from top), with ESR as wrapping material (third from top) and TYVEK (bottom). In each figure the deposited energy, calculated as $\sqrt{E_{\text{PMT1}} \cdot E_{\text{PMT2}}}$, is plotted as a function of the beam-impact position. The beam-impact position is calculated with the time difference of the PMT signals at both ends of the scintillator.

The influence of position dependence was smallest for aluminum wrapping. In case of ESR material, the behavior of energy with position is opposite to the case with no wrapping: the measured energy decreases while approaching the photomultipliers. Figure 11 also shows, that in case of all wrapping materials the measured energy is higher as compared to the case of no wrapping. This is due to photons which finally reached the PMTs after many reflections on the wrapping material. In experiments with low-photon statistics this effect is desirable. In our case, these late photons do not improve the energy resolution (as heavy-ion beams produce enough photons) but instead result in long tails in the measured energy signals [59]. These long tails do not improve the energy resolution, but they introduce pile-up at high counting rates. Thus, we have rejected any refractory material, even aluminum, as the wrapping material in order not to be limited in counting rate due to long signals.

As a final configuration, we have opted for a non-refractory light-tight 10 μm -thick black foil as a wrapping material. This option was chosen in order to avoid cross-talk between two neighbouring bars without introducing long tails in the signal shape, as in this case all photons leaving the scintillator are absorbed by the foil. The position dependence of the energy-loss signal in the case of bars wrapped with a black foil is almost identical to the case of no wrapping.

By looking at Fig. 11, one can see strong edge effects approaching the ends of the bars at +40 cm and -40 cm. In order to avoid these effects, we have decided to make the

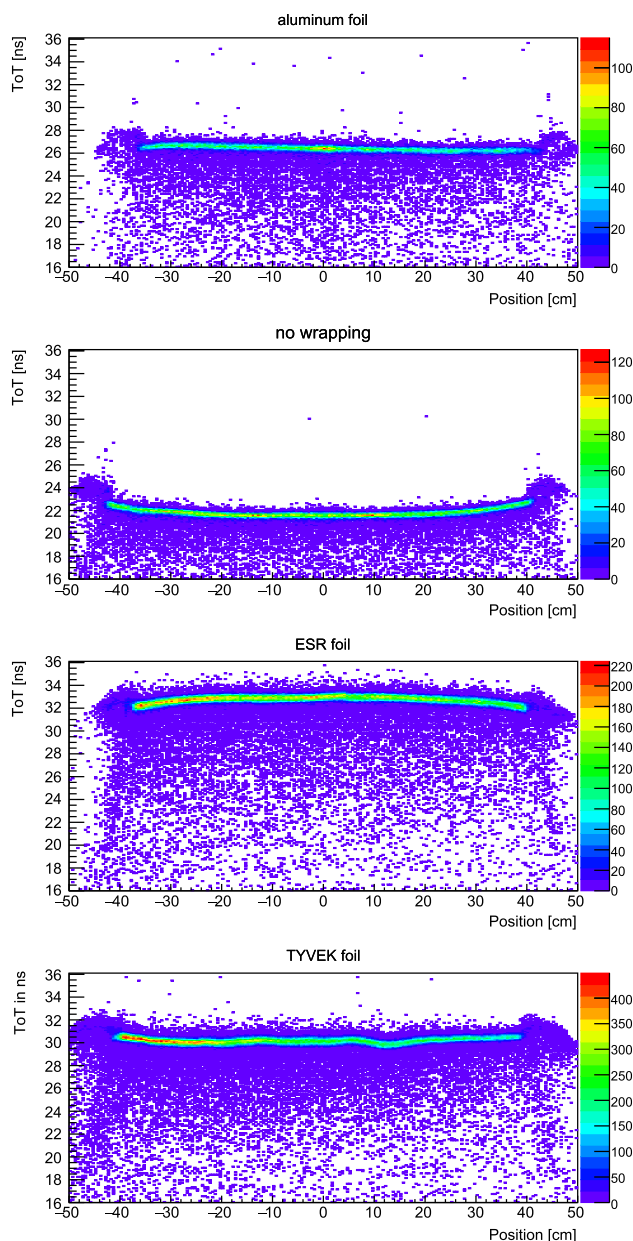


Fig. 11 Non-calibrated deposited energy as a function of the ^{48}Ca impact position for bars without any wrapping material (second from top), for bars wrapped with Al-foil (top), ESR (third from top) and TYVEK (bottom)

final detector somewhat larger than the active area required in the R³B setup by increasing the length of the bars from 80 cm (as it was in the prototype detector) to 100 cm for the final detector.

In order to correct offline for the observed position dependence of energy-loss signals, we have tested several functions [59]. The best results have been obtained by fitting a two-component exponential function to the measured energy of

Table 6 Nuclear-charge resolution measured with the new ToFD prototype and corrected for the position dependence as described in Sect. 4.2.2. Also shown (last column) is the nuclear-charge resolution required to separate Z from $Z - 1$

Beam	Energy (MeV/nucleon)	σ_Z^{exp}	σ_Z^{exp}/Z (%)	$\sigma_Z^{\text{required}}/Z$ (%)
^{48}Ca	550	0.31	1.6	2.1
^{58}Ni	500	0.19	0.68	1.5
^{124}Xe	600	0.35	0.65	0.9
^{194}Bi	700	0.34	0.41	0.6

a single PMT, as proposed in Ref. [60]:

$$E_{\text{PMT},i} = E_{\text{PMT},i}^0 \cdot \exp(-\lambda_{i,1} x_{\text{PMT},i}) + E_{\text{PMT},i}^0 \cdot \exp(-\lambda_{i,2} x_{\text{PMT},i}), \quad (16)$$

$$i = 1, 2,$$

where $E_{\text{PMT},i}^0$, $\lambda_{i,1}$, and $\lambda_{i,2}$ are fit parameters.

In this way, we improve the precision of an energy-loss measurement by a factor of 1.6 in the experiments with heavy-ion beams (see below and Table 6). Equivalent results to the above-described approach are obtained using the geometric mean and then correcting the position dependence of each bar with a polynomial of second order.

4.2.3 Tests of the prototype detector with heavy-ion beams

To test further the accuracy of the new detector concerning nuclear-charge precision for heavier beams, we have performed tests with a stable ^{124}Xe beam at 600 MeV/nucleon and a radioactive ^{194}Bi beam at 700 MeV/nucleon. The measured nuclear-charge spectra for these two cases are shown in Fig. 12. Even in case of Bi, there is a clear separation between single nuclear charges.

In Table 6 a summary of the nuclear-charge precision measured with several different heavy-ion beams during the test beam time is shown. The charge resolution was obtained by a Gaussian fit of individual peaks. It can be seen, that in all cases the design goals are met.

Please note that the measured values given in Table 6 are the “worst-case” values. In all beam tests listed above, the prototype detector was tested in a parasitic mode, at the end of the beam line in air, with many other detectors and layers of matter in front of it. These conditions do not correspond to the experimental conditions in which the ToFD detector will be used.

4.3 Time precision of the prototype detector

First tests of the timing precision of the ToFD prototype have been performed during the S438 experiment using ^{58}Ni beam

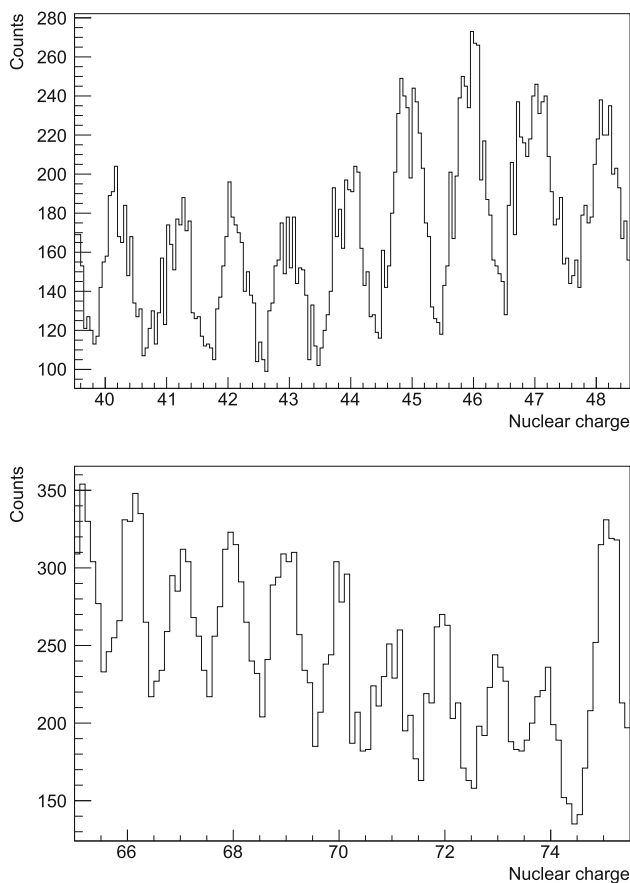


Fig. 12 Nuclear-charge spectra of reaction products from ^{124}Xe at 600 MeV/nucleon (top) and ^{194}Bi at 700 MeV/nucleon (bottom). The background present in both spectra is due to a large amount of different materials and detectors that were located in front of the ToFD prototype during the test experiments

at 500 MeV/nucleon and at various counting rates. Later, additional tests using ^{124}Xe at 600 MeV/nucleon, and ^{194}Bi (secondary beam) at 700 MeV/nucleon were performed.

For the determination of the time precision we plot the time difference of hits between the first and second plane of the detector and perform a Gaussian fit. In the case of ^{58}Ni beam at 500 MeV/nucleon with 5 kHz rate a value of $\sigma_t = 41$ ps is obtained. For an overview of all measured rates, see Table 7.

Assuming that the scintillators of the two planes have similar performance, $\sigma_t = 41/\sqrt{2}$ ps = 29 ps is obtained for the time precision of one scintillator. To estimate the performance of the full detector where the time will be measured with four planes and against a start detector with much better time precision, this value is divided by $\sqrt{4}$, yielding $\sigma_t^{\text{det}} = 14$ ps. For a flight path of 20 m, this would correspond to a relative time precision of $\sigma_t/t = 0.016\%$, which is smaller than the design goal of 0.02%. Even at 1000 kHz one could reach a time precision for the whole detector of 23 ps, which is rather close to the design goal. Please note, that the contri-

Table 7 Time precision measured with the new ToFD prototype between two bars at different counting rates for PMT signal heights of ~ 200 mV. Also shown (last column) is the time precision expected for the full detector with four planes. Data were measured with ^{58}Ni at 500 MeV/nucleon

Rate (kHz)	σ_t (ps)	σ_t^{det} (ps)
5	41	14
59	41	14
375	45	16
1000	64	23

bution from the electronics amounted to 25 ps per read-out channel in the ^{58}Ni run. The developments which took place since then have resulted in an electronic time precision of 13 ps per channel.

The measured time precision of 14 ps agrees very well with the results of simulations presented in Sect. 3.3. In the simulations, see Fig. 5, we obtain about 15 ps for low values of photoelectron threshold and about 10 ps for the higher photoelectron thresholds. This good agreement between simulation and experimental data confirms that our design goal of $\sigma_t/t = 0.02\%$ for the relative time precision can be reached with the new detector.

Table 8 summarizes the time-precision measurements of the ToFD prototype. Comparing these values with the values given in Table 1 one clearly sees that the new detector fulfills the design goals on time precision. However, one should keep in mind, that the values measured here give the intrinsic time precision of the detector. In an experiment, one needs time-of-flight information for fragments having different nuclear charges and having different velocities. Since a leading-edge discriminator is used in the electronics, the measured time-of-flight is influenced by a walk effect. Thus, although the ToFD detector has an excellent intrinsic time precision, the overall timing for all charges in the experiment depends critically on the quality of the walk correction.

5 Mechanical design

The mechanical design of the ToFD detector (see Fig. 13) foresees a modular design with two frames, each frame containing two layers of scintillator bars.

The two frames can be combined to form a light-tight housing or used individually at different positions in the setup. At the front and the rear side, the detector is closed by two end-covers holding a thin black plastic foil with a thickness of 100 μm in order to make the assembly light-tight. The frames of the ToFD detector, are quadratical and can be mounted with bars in vertical or horizontal alignment dependent on the experiment.

Table 8 Time precision between two bars of the ToFD detector. Also shown are corresponding time precisions of the whole detector, and the time precision required to separate A_{proj} from $A_{\text{proj}} - 1$ at the cor-

responding beam energy. We see, that in all cases the measured time precision of the prototype detector is better than required

Beam	Energy (MeV/nucleon)	σ_t (ps)	σ_t^{det} (ps)	$\sigma_t^{\text{required}}$ (ps)
^{58}Ni	500	41	14	235
^{124}Xe	600	31	11	75
^{194}Bi	700	22	8	31

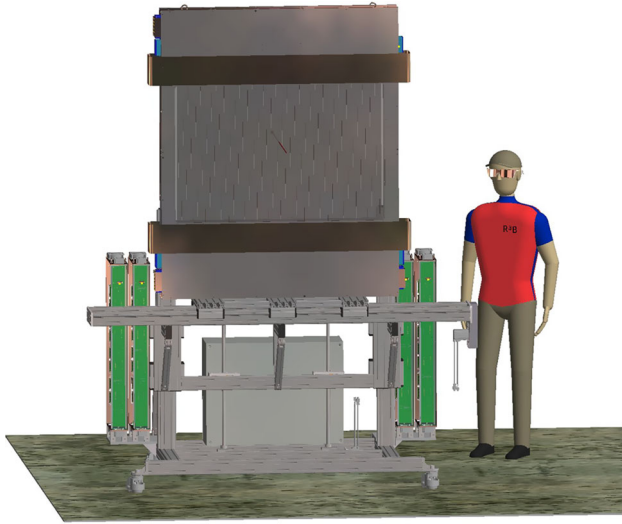


Fig. 13 Mechanical design of ToFD: The detector is mounted on an x/y -table, which allows to move the detector through the beam. In this way the position calibration, gain matching and time-offset determination can be performed. The bands at the top and bottom are made of Mu-metal and can be used for magnetic shielding of the PMTs when the detector is mounted close to the superconducting magnet GLAD. The electronics is mounted on the left and right side (green boxes)

Each plane contains 44 vertical scintillator bars with the dimensions $1000 \times 27 \times 5 \text{ mm}^3$. The bars of two successive planes are shifted by half a bar width. In this way the small gap between two bars is covered by the previous or by the next plane. Each bar is read out by PMTs on both far ends. The mounting of the PMTs and the scintillators is done in a way to ensure quick replacement if necessary. Especially for high beam rates one expects radiation damage of the bars which are hit by the unreacted beam and, therefore, a more frequent exchange of scintillators in this region is required.

The detector is positioned on a table, see Fig. 13, which allows to move the detector in the x - and y -direction. This facilitates the calibration of the whole surface of the detector with unreacted incoming beam.

The high voltage distribution is realized by CAEN multi-pin HV modules. Each module has 28 channels and 16 multi-pin connectors are distributed along the frames. The signal cables are connected to 8-fold MMX connectors, matching the 8-fold geometry of the front-ends of the readout electronics.

6 Results of the final detector

After the design studies and prototype tests, the final ToFD detector was built and used for the first time for experiments carried out during the FAIR phase-0 physics program in 2019. A calibration and analysis code was developed and included in R3BRoot [61], which is the simulation and analysis framework of the R³B collaboration. In this Chapter we want to outline the calibration procedure and show first results obtained with the new detector.

The calibration procedure consists of several steps. The beam spot of the unreacted beam on the detector is only a few cm in diameter. In a first step, the detector is moved in the x -direction through the beam and all bars are irradiated in the center. The measured spectra are analyzed and with a semi-automatic procedure the voltages of all PMTs are adjusted to obtain a similar gain.

After adjusting the HV, the detector is moved once more in x -direction through the beam. The beam hits the center of the bars and the time-offsets of all PMTs are determined in a way that the time difference between the two PMTs attached to the same bar is zero. In the same step, a time synchronisation is also done so that all bars⁴ show the same time-of-flight relative to a start detector.

Afterwards, the x/y -table is moved by a well defined distance in y -direction and with another movement in x -direction the position calibration in y -direction is obtained. The position along a bar can either be calculated by the time difference or by the ratio of the energy deposit.

Finally, the detector is moved in a meander pattern through the beam, making sure that the full length of each bar is hit by the ions. With this data the correction of the position-dependent charge measurement is performed.

After these calibration steps, which can be performed in a rather short time of a few hours, the detector is ready for the experiment. To demonstrate the performance of the detector we present results from the S473 experiment, where a stable ^{120}Sn beam at 800 MeV/nucleon impinged on a 4.5 mm thick carbon target. Both the unreacted beam and the reaction products hit the ToFD detector. The diameter of the

⁴ The time of a given bar is defined as $(t_{\text{PMT1}} + t_{\text{PMT2}})/2$, where t_{PMT1} and t_{PMT2} are times measured by the two PMTs attached to this bar.

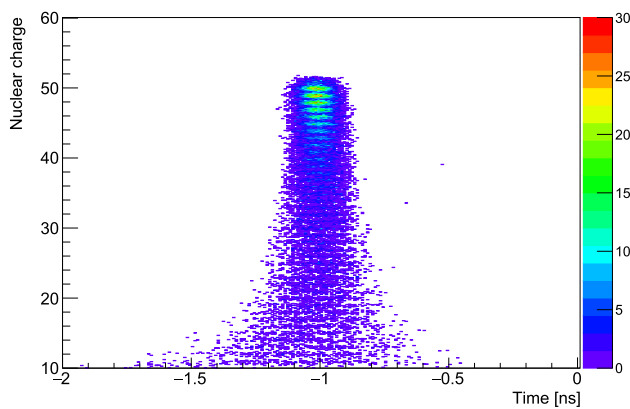


Fig. 14 The measured time difference between plane 1 and 2 for particles with different nuclear charges. A projection of selected nuclear charges on the x -axis yields the time precision. For charge 50 $\sigma_t = 37$ ps is obtained

beam spot of the unreacted beam is rather small and only a few scintillator bars in the center of the ToFD detector are hit. The reaction products are distributed over a larger area. In the current study we have selected an area which is outside of the beam spot of the unreacted beam in order to give more emphasis to the reaction products. Otherwise the spectra are dominated by contributions from the unreacted beam.

To determine the time precision, the nuclear charge of the reaction products is plotted against the time difference between plane 1 and 2 (see Fig. 14). One can see how the time precision gets worse for smaller nuclear charges which is mostly due to lower photon statistics for smaller nuclear charges. A Gaussian fit on the events with nuclear charge 50 yields a time precision of $\sigma_t = 37$ ps. This corresponds to $\sigma_t = 13$ ps for the full detector with four planes.

The electronics used for the detector has a leading-edge discriminator which results, as already mentioned, in a strong walk effect. In Fig. 14 this cannot be seen since all bars have a similar walk effect, and for time differences within the detector the effect is mostly negated. However, for the time-of-flight of the particle from the start detector to the ToFD detector this effect can be seen and the precision of the full time-of-flight measurement depends on the walk correction.

Figure 15 shows the measured nuclear-charge distribution of the fragments. An excellent nuclear-charge precision of $\sigma_Z = 0.22$ charge units or 0.44% was obtained. This can be even slightly improved by applying a velocity correction, since the fragments have a spread in velocities after a rather thick carbon target. The results were obtained by averaging the charge measurement of all 4 planes and using the bars on one side of the detector excluding the central part where the nuclear-charge spectrum is dominated by the unreacted beam particles.

In order to obtain the correct nuclear charge, the measured ToT -spectra of all bars have to be calibrated. The peaks in the spectra are located and by counting down the charge,

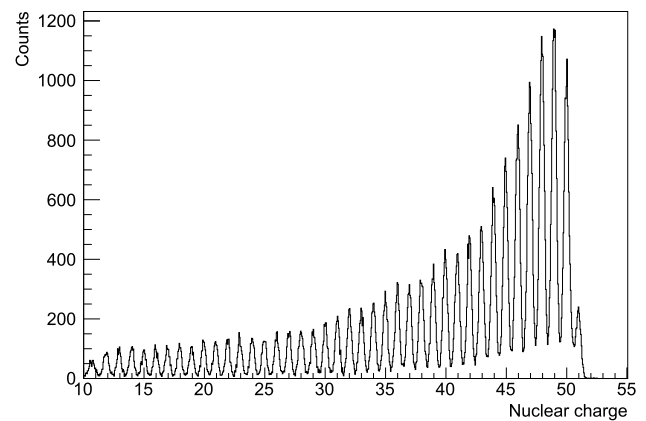


Fig. 15 Nuclear charge of the reactions products from the reactions of ^{120}Sn beam at 800 MeV/nucleon with a carbon target and measured with the new ToFD detector

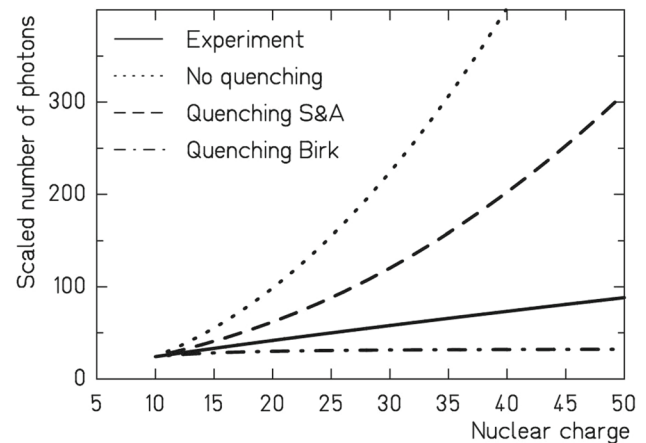


Fig. 16 Comparison of light quenching factors for Ref. [30] (dashed line), Birk's law (dash-dotted line) and measured with the reaction products of a ^{120}Sn beam (solid line). For comparison, also a quadratic function assuming no quenching is plotted (dotted black line). All lines are normalized to a nuclear charge value of 10

from the known nuclear charge of the unreacted beam, the corresponding nuclear charges are assigned. Afterwards a fit of a polynomial function of second degree is used as calibration. Since the measured ToT is proportional to the energy loss of the ions in a scintillator bar, a quadratic dependence is expected. However, as discussed in Sect. 3, quenching can reduce the light production in a scintillator. In Fig. 16 the obtained experimental function is compared with the methods used for the simulations. The measured relation between the charge from the ToT -signal and the nuclear charge is almost linear and lies between the values given in Ref. [30] and the calculation with Birk's law (see Eq. 14) used for the simulations. However, also other effects, e.g. saturation in the PMT or non-linearities in the electronics chain, can cause a similar behaviour. Therefore, not all losses can be uniquely attributed to quenching.

7 Summary

A new time-of-flight wall has been designed as part of the R^3B setup at GSI and FAIR, prototypes have been tested and the final detector has been built. The detector is used to detect and resolve nuclear-charge and mass of heavy-ion fragments up to the lead-uranium region at relativistic energies.

The detector has an active surface of $1200 \times 1000 \text{ mm}^2$, and consists of four planes of scintillators. Each plane contains 44 vertical scintillator bars with the dimensions $27 \times 1000 \times 5 \text{ mm}^3$. Each bar is read out by photomultipliers on both far ends. The width of the single bar is matched to the size of a PMT, in order to omit light guides, and couple the scintillator bars directly to the PMTs, maximizing the light collection.

First results obtained for in-beam measurements during the FAIR Phase-0 program show that the design goals - a relative energy-loss precision of $\sigma_{\Delta E}/\Delta E < 1\%$ and a relative time precision of $\sigma_t/t < 0.02\%$ - are fully met. This will allow, together with an elaborate particle-tracking system, the full identification of heavy-ions up to the lead-uranium region in mass and nuclear charge.

Acknowledgements The results presented here have been measured at the GSI Helmholtzzentrum für Schwerionenforschung, Darmstadt, Germany. Part of the data was obtained during the FAIR Phase-0 experiment S473 with the R^3B experimental setup situated at the HTC. All results presented here have been obtained before 24th February, 2022. This work received support from BMBF (05P19RFFN1, 05P15RDFN1, 05P19RDFN1) and HIC for FAIR. J.P. has been supported by the Institute for Basic Science (IBS-R031-D1). E.C. has been supported by the Ministry of Science and Innovation in Spain (PGC2018-099746-B-C22). J.L.R.S. thanks the support from the Regional Government of Galicia under the program of postdoctoral fellowships ED481B-2017-002 and ED481D-2021-018. O.T. has been supported by AEI/FEDER, UE project No. PID2019-104390GB-I00. G.B., A.H., H.T.J., B.J. and T.N. have been supported by the Swedish Research Council under contract 2017-03839. This work was supported by the Royal Society and UK STFC awards ST/L005727/1, ST/P003885/1. R^3B members: Current information according to the NUSTAR database: Marialuisa Aliotta, Georgy Alkhazov, Tahani Almusidi, Hector Alvarez-Pol, Paul André, Marlène Assié, Leyla Atar, Liam Atkins, Laurent Audouin, Thomas Aumann, Gilles Authalet, Yassid Ayyad, Martin Bajzek, Antoine Barriere, Saul Beceiro-Novo, Sergey Belogurov, Daniel Bemmerer, Jose Benlliure, Carlos Bertulani, Andrey Bezbakh, Guillaume Blanchon (observer), Carl Georg Boos, Konstanze Boretzky, Maria J. Borge, Ivan Borzov, Lukas Bott, Benjamin Brückner, Pablo Cabanelas Eiras, Christoph Caesar, Stefana Calinescu, Enrique Casarejos, Wilton Catford, Joakim Cederkall, Audrey Chatillon, Madalin Ilie Cherciu, M Majid Rauf Chishti, Leonid Chulkov (observer), Andreea Cirstian, Anna Corsi, Dolores Cortina-Gil (Spokesperson), Edgar Cravo, Raquel Crespo, Andrey Danilov, Giacomo de Angelis, Enrico De Filippo, Alexis Diaz-Torres, Timo Dickel, Alexander Dobrovolsky, Pieter Doornenbal, Meytal Duer, Peter Egelhof, Zoltan Elekes, Joachim Enders, Philipp Erbacher, Sonia Escribano Rodriguez, Claes Fahlander (observer), Ashton Falduto, Martina Feijoo, Daniel Fernandez Ruiz, Andrey Fomichev, Zsolt Fulop, Daniel Galaviz Redondo, Elisabet Galiana, Gabriel García, Vicente García Távara, Igor Gasparic, Zhuang Ge (observer), Hans Geissel, Elena Geraci, Jürgen Gerl, Roman Gernhäuser, Alain Gillibert, Jan Glorius, Brunilde Gnoffo, Kathrin Göbel,

Mikhail Golovkov (observer), Victor Golovtsov, Pavel Golubev, David González Caamaño, Alexander Gorshkov, Antia Graña González, Anatoly Gridnev, Nikolai Gruzinskii, Valdir Guimaraes, Muhsin N. Harakeh, Anna-Lena Hartig, Tanja Heftrich, Henning Heggen, Michael Heil, Andreas Heinz, Or Hen, Corinna Henrich, Ana Henriques, Thomas Hensel, Matthias Holl, Ilja Homm, Andrea Horvat, Ákos Horváth, Jan-Paul Hucka, Alexander Inglessi, Andrea Jedeke, Desa Jelavic Malenica, Tobias Jenegger, Liancheng Ji, Håkan Johansson, Björn Jonson, Beatriz Jurado, Julian Kahlbow, Nasser Kalantar-Nayestanaki, Armel Kamenyero, Erika Kazantseva, Aleksandra Kelic-Heil, Alexey Khanzadeev, Oleg Kiselev, Philipp Klenze, Alexander Knyazev, Karsten Koch, Moschos Kogimtzis, Kei Kokubun, Guerman Korolev, Daniel Körper, Alexey Korshennikov, Wolfram Korten, Nikolai Kozlenko, Sabina Krasilovskaja, Dmytro Kresan, Anatoly Krivshich, Thorsten Kröll, Sergey Krupko, Eleonora Kudaibergenova, Dorottya Kunne Sohler, Deniz Kurtulgil, Nikolaus Kurz, Evgeny Kuzmin, Viacheslav Kuznetsov, Marc Labiche, Andrea Lagni, Christoph Langer, Zsombor Lányi, Ian Lazarus, Arnaud Le Fèvre, Yvonne Leifels, Alinka Lepine-Szily, Marek Lewitowicz, Ivana Lihtar, Bui Linh, Yuri Litvinov, Hongna Liu, Bastian Löher, Bettina Lommel, Enis Lorenz, Jerzy Lukasik, Augusto Macchiavelli, Evgeny Maev, Charles Maillert, Dmitrii Maisuzenko, Adam Maj, Nunzia Simona Martorana, Benoît Mauss, Christophe Mayri, Leandro Milhomens da Fonseca, Pierre Morfouace, Nikhil Mozumdar, Dennis Mücher (observer), Silvia Murillo Morales, Enrique Nacher, Evgenii Nikolskii, Thomas Nilsson, Chiara Nociforo, Fritz Nolden, Göran Nyman (observer), Alexandre Obertelli, Emanuele Vincenzo Pagano, Valerii Panin, Joochun Park, Stefanos Paschalis, Junchen Pei, Angel Perea, Marina Petri, Eli Piasetzky, Stephane Pietri, Sara Pirrone, Giuseppe Politi, Emanuel Pollacco (observer), Lukas Ponnath, Petru-Mihai Potlog, Rinku Prajapat, Roman Pritula, Hang Qi, Christophe Rappold, Rene Reifarh, Aldric Revel, Han-Bum Rhee, Fabio Risitano, Jose Luis Rodriguez Sanchez, Luke Rose, Dominic Rossi, Matthias Rudigier, Paolo Rusotto, Ángel-Miguel S*ánchez-Benítez, Shahab Sanjari, Clementine Santamaria, Victor Sarantsev, Deniz Savran, Christoph Scheidenberger, Heiko Scheit (Project Manager), Konrad Schmidt, Haik Simon (Deputy Spokesperson), Johannes Simon, Zuzana Slavkovská, Roman Slepnev (observer), Olivier Sorlin, Tomás Sousa, Alexandra Spiridon, Emil Stan, Mihai Stanoiu, Alexandra Stefanescu, Ionut Stefanescu, Sonja Störck-Dutine, Aaron Stott, Baohua Sun (observer), Yelei Sun, Christian Sürder, Julien Taieb, Junki Tanaka, Isao Tanihata, Ryo Taniuchi, Olof Tengblad (Technical Director), Pavel Terekhin, Pamela Teubig, Hans Törnqvist, Livius Trache, Wolfgang Trautmann, Marina Trimarchi, Stefan Typel (observer), Tomohiro Uesaka, Carl Unsworth (observer), Lev Uvarov, Marine Vandebrouck, Laszlo Varga, Simone Velardita, Paulo Velho, Matjaz Vencelj, Meiko Volknandt, Sergei Volkov, Martin von Trescow, Andreas Wagner, Felix Wamers, Yanzhao Wang, Matthew Whitehead, Frank Wienholtz, Kathrin Wimmer, Martin Winkler, Manuel Xarepe, Yanlin Ye, Sabrina Zacarias, Juan Carlos Zamora Cardona, Wei Zhang, Andrei Zhdanov, Mikhail Zhukov (observer), Andreas Zilges, Kai Zuber.

Funding Information Open Access funding enabled and organized by Projekt DEAL.

Data Availability Statement This manuscript has no associated data or the data will not be deposited. [Author's comment: Raw data were generated at GSI. Derived data supporting the findings of this study are available from the corresponding author M.H. on request.]

Open Access This article is licensed under a Creative Commons Attribution 4.0 International License, which permits use, sharing, adaptation, distribution and reproduction in any medium or format, as long as you give appropriate credit to the original author(s) and the source, provide a link to the Creative Commons licence, and indicate if changes were made. The images or other third party material in this article are included in the article's Creative Commons licence, unless indi-

cated otherwise in a credit line to the material. If material is not included in the article's Creative Commons licence and your intended use is not permitted by statutory regulation or exceeds the permitted use, you will need to obtain permission directly from the copyright holder. To view a copy of this licence, visit <http://creativecommons.org/licenses/by/4.0/>.

References

1. H. Geissel et al., Nucl. Instrum. Methods B **204**, 71 (2003)
2. M. Winkler et al., Nucl. Instrum. Methods B **266**, 4183 (2008)
3. R. Palit et al., Phys. Rev. C **68**, 034318 (2003)
4. <https://www.gsi.de/glad.htm>. Accessed 25 July 2022
5. M. Borri et al., Nucl. Instrum. Methods A **836**, 105 (2016)
6. Technical Report for the Design, Construction and Commissioning of the CALIFA Barrel: The R3B CALorimeter for In Flight detection of gamma rays and high energy charged particles. <https://edms.cern.ch/document/1833500/1>. Technical Report for the Design, Construction and Commissioning of the CALIFA endcap. <https://edms.cern.ch/document/1833748/1>. Accessed 25 July 2022
7. K. Boretzky, et al., Nucl. Instrum. Methods A **1014**, 165701 (2021). Technical Report for the Design, Construction and Commissioning of NeuLAND. <https://edms.cern.ch/document/1865739/1>. Accessed 25 July 2022
8. Technical report for the design, construction and commissioning of the tracking detectors for R3B. <https://edms.cern.ch/document/1865815/1>
9. R³B Letter-of-Intent. A universal setup for kinematical complete measurements of reactions with relativistic radioactive beams (R³B)
10. J. Allison et al., Nucl. Instrum. Methods A **835**, 186 (2016)
11. R.F. Post, L.I. Schiff, Phys. Rev. **80**, 1113 (1950)
12. P. Achenbach et al., Nucl. Instrum. Methods **A578**, 253 (2007)
13. E. Gatti, V. Svetlo, Nucl. Instrum. Methods **30**, 213 (1964)
14. L.G. Hyman, Rev. Sci. Instrum. **36**, 193 (1965)
15. E. Gatti, V. Svetlo, Nucl. Instrum. Methods **43**, 248 (1966)
16. S. Donati, E. Gatti, V. Svetlo, Nucl. Instrum. Methods **46**, 165 (1967)
17. B. Sigfridsson, Nucl. Instrum. Methods **54**, 13 (1967)
18. M. Bertolaccini et al., Nucl. Instrum. Methods **51**, 325 (1967)
19. Yu.K. Akimov, S.V. Medved, Nucl. Instrum. Methods **78**, 151 (1970)
20. M. Moszynski, B. Bengtson, Nucl. Instrum. Methods **158**, 1 (1979)
21. I. Sazanov, M. Kelbert, A.G. Wright, Nucl. Instrum. Methods **A572**, 804 (2007)
22. Y. Shao, Phys. Med. Biol. **52**, 1103 (2007)
23. S. Seifert, H.T. van Dam, D.R. Schaart, Phys. Med. Biol. **57**, 1797 (2012)
24. B. Bengtson, M. Moszynski, Nucl. Instrum. Methods **81**, 109 (1970)
25. B. Bengtson, M. Moszynski, Nucl. Instrum. Methods **117**, 227 (1974)
26. T. Batsch, B. Bengtson, M. Moszyński, Nucl. Instrum. Methods **125**, 443 (1975)
27. M. Moszynski, B. Bengtson, Nucl. Instrum. Methods **142**, 417 (1977)
28. N.P. Hawkes, G.C. Taylor, Nucl. Instrum. Methods A **729**, 522 (2013)
29. <http://web-docs.gsi.de/~weick/atima/>. Accessed 25 July 2022
30. M.H. Salomon, S.P. Ahlen, Nucl. Instrum. Methods **195**, 557 (1982)
31. <http://www.eljentechnology.com>. Accessed 25 July 2022
32. J. Allison, et al., Nucl. Instrum. Methods **A835**, 186 (2016) (and ref. therein)
33. B.L. Leverington, et al. [arXiv:1106.5649v2](https://arxiv.org/abs/1106.5649v2) [physics.ins-det]. <https://doi.org/10.15161/oar.it/1449018198.02>
34. K. Koch, et al., IEEE Trans. Nucl. Sci. **52**, 745 C. Caesar et al., "Heading towards FAIR: upgrades on the R3B-Cave C electronics", GSI Scientific Report p. 310 (2009)
35. J. Frühauf, J. Hoffmann, E. Bayer, N. Kurz, GSI Scientific Report, p. 300 (2012)
36. C. Ugur, E. Bayer, N. Kurz, M. Traxler, J. Instrum. C02004–C02004 (2012)
37. A. Schüttauf et al., Nucl. Instrum. Methods **533**, 65 (2004)
38. A. Schüttauf et al., Nucl. Phys. B Proc. Suppl. **158**, 52 (2006)
39. M. Ciobanu et al., IEEE Trans. Nucl. Sci. **54**, 1201 (2007)
40. K. Koch, H. Simon, C. Caesar, GSI Scientific Report, p. 235 (2010). <https://doi.org/10.15120/GR-2015-1-MU-NUSTAR-NR-14>
41. Z. Deng, et al., IEEE Trans. Nucl. Sci. **57**, 3212 (2011) (and refs. therein)
42. C. Paul, et al., IEEE Trans. Nucl. Sci. **59**, 1809 (2012) (and refs. therein)
43. M. Ciobanu et al., IEEE Trans. Nucl. Sci. **61**, 1015 (2014)
44. C. Ugur, et al., GSI Scientific Report, p. 204 (2014). <https://doi.org/10.15120/GR-2015-1-MU-NUSTAR-NR-14>
45. Karsten Koch, private communication (2017)
46. H. Nishino et al., Nucl. Instrum. Methods **A610**, 710 (2009)
47. http://psec.uchicago.edu/links/pmt_handbook_complete.pdf. Accessed 25 July 2022
48. Hamamatsu Photonics K.K., Hamamatsu photomultiplier tube R8619 (2014). http://www.hamamatsu.com/resources/pdf/etd/R8619_TPMH1331E.pdf. Accessed 25 July 2022
49. V. Kalinnikov et al., Instrum. Exp. Tech. **49**, 223 (2006)
50. J. Gerbig, "Kalibrierung eines Szintillationsdetektors mit Hilfe von LEDs", Masterarbeit 2013, Goethe-Universität Frankfurt/Germany; urn:nbn:de:hebis:30:3-337392
51. OSRAM Opto Semiconductors GmbH: Hyper-Bright LED LB Q39E (2012)
52. http://www.users.ts.infn.it/~rui/univ/Acquisizione_Dati/Manuals/LRS%209210.pdf. Accessed 25 July 2022
53. N. Kurz, "VFTX2", EPAC'96, Sitges, June 1996, p. 7984
54. R. Perrino et al., Nucl. Instrum. Methods **A381**, 324 (1996)
55. A. Khodaparast, "Charakterisierung eines szintillator-basierten Flugzeitdetektors", Bachelorarbeit 2016, Goethe-Universität Frankfurt/Germany
56. <http://www.picoquant.com/products/category/picoquant-pulsed-driver/pdl-800-d-picoquant-pulsed-diode-laser-driver-with-cw-capability>. Accessed 25 July 2022
57. DuPont. <http://www.dupont.com>, Tyvek is a DuPont registered trademark. Accessed 25 July 2022
58. www.3m.com/3M/en_US/company-us/all-3mproducts/~/3M-Enhanced-Specular-Reflector-3MESR-/?N=5002385+3293061534&rt=rud. Accessed 25 July 2022
59. M. Gilbert, "Aufbau einer ToF-Wall für R³B", Masterarbeit 2014, Goethe-Universität Frankfurt/Germany; urn:nbn:de:hebis:30:3-365905
60. M. Taiuti et al., Nucl. Instrum. Methods A **370**, 429 (1996)
61. D. Bertini, M. Al-Turany, I. Koenig, F. Uhlig, The FAIR simulation and analysis framework. Journal of Physics Conference Series **119**(3), 032011 (2008). <https://doi.org/10.1088/1742-6596/119/3/032011>